HHS Public Access

Author manuscript

Cell Rep. Author manuscript; available in PMC 2022 November 15.

Published in final edited form as:

Cell Rep. 2022 September 27; 40(13): 111429. doi:10.1016/j.celrep.2022.111429.

Impad1 and Syt11 work in an epistatic pathway that regulates EMT-mediated vesicular trafficking to drive lung cancer invasion and metastasis

Rakhee Bajaj[1,2], **B. Leticia Rodriguez**[1], **William K. Russell**[4], **Amanda N. Warner**[1,2], **Lixia Diao**[5], **Jing Wang**[5], **Maria G. Raso**[6], **Wei Lu**[6], **Khaja Khan**[6], **Luisa S. Solis**[6], **Harsh Batra**[6], **Ximing Tang**[6], **Jared F. Fradette**[1,2], **Samrat T. Kundu**[1], **Don L. Gibbons**[1,3,7,*]

[1]Department of Thoracic/Head and Neck Medical Oncology, University of Texas MD Anderson Cancer Center, 1515 Holcombe Boulevard, Houston, TX 77030, USA

[2]UTHealth Graduate School of Biomedical Sciences, University of Texas MD Anderson Cancer Center, 6767 Bertner Avenue, Houston, TX 77030, USA

[3]Department of Molecular and Cellular Oncology, University of Texas MD Anderson Cancer Center, Houston, TX 77030, USA

[4]Department of Biochemistry and Molecular Biology, University of Texas Medical Branch, Galveston, TX 77555, USA

[5]Department of Bioinformatics and Computational Biology, University of Texas MD Anderson Cancer Center, Houston, TX 77030, USA

[6]Department of Translational Molecular Pathology, University of Texas MD Anderson Cancer Center, 1515 Holcombe Boulevard, Houston, TX 77030, USA

[7]Lead contact

SUMMARY

Lung cancer is a highly aggressive and metastatic disease responsible for approximately 25% of all cancer-related deaths in the United States. Using high-throughput *in vitro* and *in vivo* screens, we have previously established Impad1 as a driver of lung cancer invasion and metastasis. Here we elucidate that Impad1 is a direct target of the epithelial microRNAs (miRNAs) miR-200

*Correspondence: dlgibbon@mdanderson.org.

AUTHOR CONTRIBUTIONS

Study conceptualization, design, and execution of project, R.B. and D.L.G.; data acquisition and statistical analysis, R.B., B.L.R., and A.N.W.; mass spectrometry, W.K.R.; bioinformatics analysis for mRNA and miRNA correlations in human cell lines and tumors, L.D. and J.W.; IHC on human lung cancer specimens, W.L., K.K., and L.S.S.; digital image analysis, H.B.; mouse model generation and maintenance, J.F.F. and S.T.K.; overall supervision of IHC staining, M.G.R.; analysis, interpretation, and representation of data, R.B.; manuscript writing, critical revision, and preparation of figures and tables, R.B., J.F.F., A.N.W., and D.L.G.; overall supervision and execution, D.L.G.

DECLARATION OF INTERESTS

D.L.G. declares advisory board work for AstraZeneca, Eli Lilly, Menarini Richerche, 4D Pharma, and Sanofi. D.L.G. has received research grant funding from AstraZeneca, Janssen, Astellas, Ribon Therapeutics, NGM Biotherapeutics, and Takeda.

SUPPLEMENTAL INFORMATION

Supplemental information can be found online at https://doi.org/10.1016/j.celrep.2022.111429.

and miR~96 and is de-repressed during epithelial-to-mesenchymal transition (EMT); thus, we establish a mode of regulation of the protein. Impad1 modulates Golgi apparatus morphology and vesicular trafficking through its interaction with a trafficking protein, Syt11. These changes in Golgi apparatus dynamics alter the extracellular matrix and the tumor microenvironment (TME) to promote invasion and metastasis. Inhibiting Impad1 or Syt11 disrupts the cancer cell secretome, regulates the TME, and reverses the invasive or metastatic phenotype. This work identifies Impad1 as a regulator of EMT and secretome-mediated changes during lung cancer progression.

In brief

Metastasis remains the primary cause of cancer-related deaths, and a better understanding of the process will determine new therapeutic avenues. Bajaj et al. show that the Golgi apparatus and Golgi apparatus-associated proteins play a key role in determining tumor metastasis, indicating the importance of targeting the organelle during cancer.

Graphical abstract

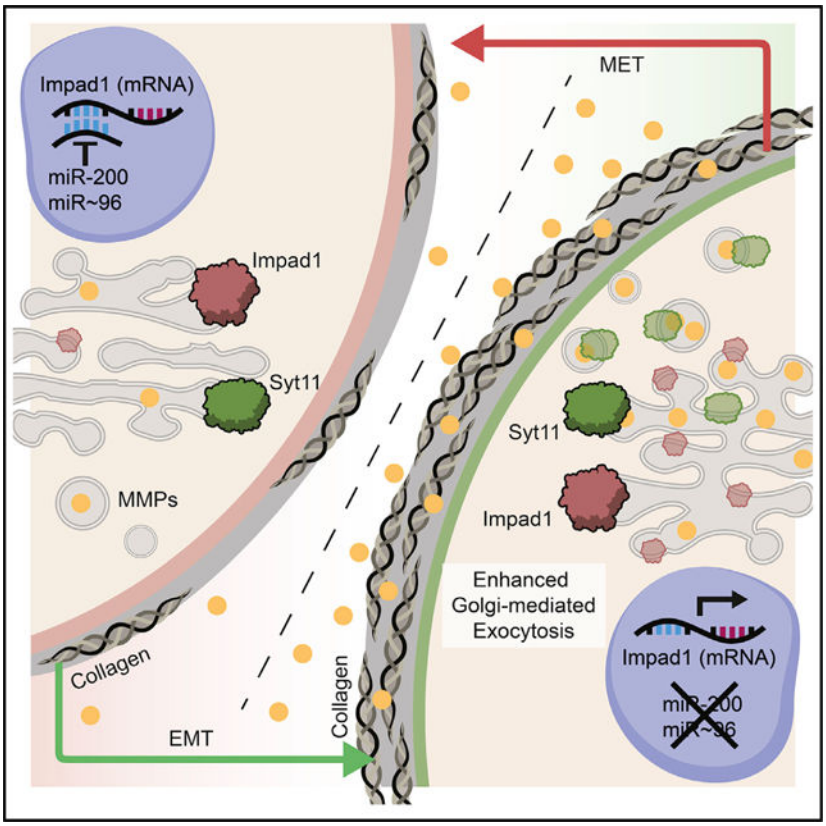

INTRODUCTION

Non-small cell lung cancer (NSCLC) is the deadliest form of cancer worldwide, primarily because of its propensity to metastasize (Siegel et al., 2021). Treating or preventing metastasis holds potential for improving survival but requires a deeper understanding of the underlying drivers and processes (Eccles et al., 2017; Steeg and Theodorescu,

2008). Our previously published high-throughput functional screens identified inositol mono-phosphatase domain-containing 1 (Impad1) as a key driver of invasion and metastasis in NSCLC (Bajaj et al., 2020; Grzeskowiak et al., 2018; Kundu et al., 2018). We established Impad1 as a Golgi apparatus-resident protein that alters Golgi apparatus mediated exocytosis of matrix metalloproteases (MMPs) to drive invasion (Bajaj et al., 2020). However, the role of Impad1 in altering Golgi apparatus dynamics and exocytosis is not yet understood.

In addition to genetic drivers of metastasis, there are also epigenetic processes that promote cancer. One such process is the epithelial-to-mesenchymal transition (EMT), which confers plasticity and fitness to cancer cells, promoting their survival throughout the metastatic cascade (Kalluri and Weinberg, 2009). This cascade and EMT are initiated by loss of epithelial microRNAs (miRNAs) such as the miRNA-200 family (miR-200) and the miR-183~96~182 cluster (miR~96), allowing their targets to be de-repressed in mesenchymal cells (Gregory et al., 2008; Kundu et al., 2016, 2022). Targets such as Zeb1 and Foxf2 are upregulated in lung cancer and drive metastasis (Gibbons et al., 2009a; Larsen et al., 2016; Kundu et al., 2016), highlighting a mode of regulation for oncogenes. However, inhibiting Zeb1 or supplementing epithelial miRNAs to regulate EMT and treat metastasis has posed pharmacological challenges (Nieto et al., 2016). This requires a better understanding of the processes downstream of EMT that drive metastasis and can be selectively inhibited in mesenchymal cells.

In line with that, Tan et al. (2017, 2020) have shown that the Golgi apparatus (Golgi) functions are modulated during Zeb1-mediated EMT to the invasive front of the tumors. Altered Golgi dynamics and heightened trafficking are hallmarks of metastatic cells, where they promote secretion of components like MMPs, collagens, glycosaminoglycans (GAGs), cytokines, and so forth into the extracellular space, priming the tumor microenvironment (TME) for malignant progression (Goldenring, 2013; Howley and Howe, 2018; Bajaj et al., 2022). However, the drivers that coordinate EMT- and metastasis-associated Golgi and secretome changes are not clear. Efforts to inhibit Golgi secretion have so far been unsuccessful for treating lung cancer in the clinic (Mughees et al., 2020; Ojha and Amaravadi, 2017; Bajaj et al., 2022). Improving our understanding of the regulators of Golgi integrity and exocytosis during EMT will aid in impeding this dynamic process to treat or prevent metastatic disease.

In this study, we delve further into the mechanism of action of Impad1 as a metastasis driver by answering two important questions: how is Impad1 upregulated in NSCLC, and how does Impad1 enhance Golgi exocytosis to promote NSCLC metastasis? We have identified Impad1 as a direct target of miR-200 and miR~96, where its expression is de-repressed because of loss of these epithelial miRNAs during EMT. Extensive mechanistic work determined that Impad1 alters Golgi dynamics by promoting a more connected and stacked Golgi as well as heightened vesicular trafficking to the plasma membrane. Using immunoprecipitation (IP)-mass spectrometry (MS), we identified the Impad1 interactome, where Impad1 interacts with another trafficking protein, Synaptotagmin XI (Syt11), and regulates Golgi-mediated exocytosis and the ability of the cancer cell secretome to orchestrate a pro-invasive and pro-metastatic TME. Inhibiting Impad1 or disrupting this epistatic pathway abrogated secretion, lung cancer invasion, and metastasis.

RESULTS

Impad1 is upregulated during EMT to promote tumorigenesis

EMT is an epigenetically regulated process that promotes tumorigenesis and metastasis (Kalluri and Weinberg, 2009; Thiery et al., 2009). Previously, our lab and others have established that human and mouse lung cancer cell lines and tumors can be distinguished based on their EMT status (Ahn et al., 2012; Gibbons et al., 2009a, 2009b). These mesenchymal-like (mesenchymal) cells and tumors are more metastatic compared with their epithelial counterparts. According to the TCGA lung adenocarcinoma dataset, Impad1 is altered in 18% of affected individuals, similar to *Kras* and *Tp53* mutations (Figure S1A). These individuals primarily demonstrate mRNA upregulation of the gene, indicating that Impad1 potentially undergoes an epigenetic modulation. To study this, we used human and mouse NSCLC cell line panels that were stratified based on the inherent EMT status. Impad1 was upregulated in mesenchymal malignant cells, correlating with the EMT markers; i.e., increased Zeb1 and reduced E-cadherin expression (Figures 1A, 1B, and S1B). Impad1 mRNA expression was also positively associated with a previously established 76-gene EMT signature (Byers et al., 2013) in 118 human NSCLC lines (Mcmillan et al., 2018; Figure 1C). IHC staining for Impad1 and Zeb1 in NSCLC tumor tissue confirmed this correlation at the protein level (Figures 1D and S1C). To investigate whether this phenomenon can be mediated by other inducers of EMT, we treated the murine KP (393P and 344SQ) as well as the murine mammary epithelial (NMuMG) cell lines with transforming growth factor β1 (TGF-β1), a cytokine that induces Zeb1 expression and EMT (Gibbons et al., 2009a). Regardless of the species, tissue of origin, baseline EMT status of the cells, and type of induction, Impad1 was upregulated during EMT (Figures 1E, 1F, and S1D).

Impad1 is a direct target of the epithelial miRNAs miR-200 and miR~96

Previous work has shown that Zeb1 and epithelial miRNAs such as the miRNA-200 family (miR-200) and the miR-183~96~182 cluster (miR~96) are part of a double-negative feedback loop that regulates EMT in cancer (Gregory et al., 2008; Kundu et al., 2016, 2022). We have also demonstrated that Zeb1 positively correlates with EMT in the previously described murine and human cancer models, whereas miR-200 and miR~96 show a negative association. Oncogenes such as Zeb1 and Foxf2, which are targets of the epithelial miRNAs, are de-repressed upon loss of these miRNAs during EMT, driving invasion and metastasis (Gibbons et al., 2009a; Kundu et al., 2016; Larsen et al., 2016). Hence, we questioned a similar modulation of Impad1 in our system during EMT. An *in silico* analysis using TargetScan identified multiple well-conserved miR-200 and miR~96 seed sequences in the Impad1 3’ UTR (Figure S2A). Bracken et al. (2014) discovered Impad1 to be a direct target of miR-200b using an Ago-HITSCLIP pull-down in breast cancer cells (Bracken et al., 2014). To investigate this in lung cancer, we used doxycycline-inducible models where Zeb1 drives EMT in epithelial 393P (murine) and H441 (human) lung cancer cells, and miR-200 or miR~96 individually induce mesenchymal-to-epithelial transition (MET) in mesenchymal 344SQ (murine) and H157 (human) cells (Peng et al., 2019). These Zeb1-inducible cell lines are more invasive, whereas epithelial miRNA induction disrupts the invasiveness of the mesenchymal cells. Like Zeb1, Impad1 was repressed

during miR-200- or miR~96-mediated MET and enhanced upon Zeb1-mediated EMT (Figures 2A–2D and S2B–S2H). Next we studied this mode of regulation of Impad1 in genetically engineered mouse models (GEMMs) of lung adenocarcinoma that recapitulate the disease progression in affected individuals (Padhye et al., 2021; Peng et al., 2019; Kundu et al., 2022; Ahn et al., 2012; Gibbons et al., 2009a, 2009b). Briefly, miR-200 (miR-200c$^{fl/fl}$) or miR~96 (miR~96c$^{fl/fl}$) conditional floxed mice were crossed with the previously described KRAS (KRAS$^{LSL\text{-}G12D/+}$) or KP (KRAS$^{LSL\text{-}G12D/+}$;p53$^{fl/fl}$) mice to generate KRAS$^{LSL\text{-}G12D/+}$;miR-200c$^{fl/fl}$ (KM200), KRAS$^{LSL\text{-}G12D/+}$; p53$^{fl/fl}$;miR-200c$^{fl/fl}$ (KPM200), and KRAS$^{LSL\text{-}G12D/+}$;miR~96c$^{fl/fl}$ (KM96) GEMMs. The conditional alleles were activated by using the Ad5-CMV-Cre driver, including KRAS$^{LSL\text{-}G12D/+}$, which was used as the control. KM, KPM200, and KM96 mice developed tumors that were heterogeneous and mesenchymal compared with the KRAS and KP tumors. EMT was validated in the tumors, as shown by high Zeb1 and low E-cadherin levels (Figure S2I), and syngeneic cell lines were also derived from KPM200 tumors to further explore EMT. Impad1 was upregulated in KM200, KM96, and KPM200 tumors compared with KRAS and KP tumors, as quantified by IHC (Figures 2E, S2I, and S2J). Cell lines derived from KP and KPM200 tumors that are more mesenchymal compared with KP epithelial cells also showed higher Impad1 expression (Figures S2K–S2M). Next we also investigated this miRNA-mediated suppression of Impad1 in the previously mentioned human NSCLC cell line (Mcmillan et al., 2018) and tumor (TCGA-Firehose legacy) datasets. Impad1 negatively correlated with miR-200 family members and miR-96 (Figures 2F, 2G, and S2N–S2T). Thus, our data established that Impad1 is upregulated during EMT upon loss of the epithelial miRNAs miR-200 and miR~96.

To ascertain whether Impad1 is a direct target of miR-200 and miR~96, we performed a 3’ UTR luciferase reporter assay with the Impad1 3’ UTR containing the wild-type or mutant miRNA seed sequences. miR-200b/c and miR-96/183 significantly repressed luciferase activity, which was rescued when the miRNA binding sites were mutated (Figures 2H, 2I, S2U, and S2V), indicating that Impad1 is a direct target of miR-200b/c and miR-96/183.

Impad1 alters the secretome of lung cancer cells undergoing EMT

We have determined previously that Impad1 is a Golgi-resident protein that drives invasion and metastasis by enhancing Golgi-mediated exocytosis of MMPs (Bajaj et al., 2020). However, inhibition of MMP activity using ilomastat did not completely abrogate Impad1-mediated invasion in 3D collagen/Matrigel matrix assays. This suggested that Impad1 likely regulates the secretion of additional extracellular factors. Given that mesenchymal cancer cells secrete proteins differentially compared with epithelial cells, EMT may drive malignancy by orchestrating the secretome changes that regulate the ECM and TME. Reka et al. (2014) performed GeLC-tandem MS and identified the secretome signature for cancer cells undergoing TGF-β-induced EMT, which predicted survival (Reka et al., 2014). Our lab has shown that Zeb1-mediated EMT enhances collagen deposition, which is associated with cancer metastasis and poor survival (Peng et al., 2017; Ungewiss et al., 2016). However, there is still a gap in understanding the comprehensive secretome of lung cancer cells undergoing EMT or how Golgiassociated proteins like Impad1 affect these changes in the mesenchymal cell secretome.

Hence, we investigated whether Impad1 plays a role in altering the secretome of lung cancer cells during EMT. We performed liquid chromatography-tandem MS (LC-MS/MS) analysis on conditioned medium (CM) collected from the epithelial 393P vector and Impad1-expressing cells as well as the mesenchymal 344SQ scramble control and Impad1 knockdown cells. We triangulated hits that were higher in Impad1-overexpressing cells compared with the vector control, lower in Impad1 knockdown cells compared with the scramble control, and higher in mesenchymal 344SQ scramble control compared with the epithelial 393P vector control (Figure 3A; Table S1). This unbiased approach identified approximately 150 proteins (≥2 peptides per protein, 1% false discovery rate) that were enhanced in the secretome of Impad1-overexpressing cells. Of these candidates, 43 (B+D) were decreased upon Impad1 knockdown, and 130 (A+D) were upregulated during EMT. This high level of overlap of the extracellular components between Impad1-overexpressing and mesenchymal cells suggested a role of Impad1 in regulating the enhanced secretion observed during EMT. However, we focused on the 32 (D) proteins that were common across all three comparisons, which included extracellular factors that have key roles in promoting cancer: collagen (Col12α1), heparanase (Hpse), Sortilin receptor (Sorl1), keratin (Krt5), glycohydrolases (Parg), and so forth. Of these, we further studied collagen because loss of Impad1 has been associated with decreased bone and cartilage ECM formation in diseases such as chondrodysplasia (Frederick et al., 2008; Sohaskey et al., 2008; Vissers et al., 2011). We have shown previously that collagen deposition is enhanced in mesenchymal metastatic tumors (Peng et al., 2017; Ungewiss et al., 2016); however, its mode of regulation remains unclear. Hence, we investigated whether Impad1 upregulation during EMT is responsible for promoting collagen deposition in the TME. We probed for collagen in syngeneic metastatic tumors overexpressing Impad1 or non-metastatic tumors with suppression of Impad1 by using Masson trichrome staining and second harmonic generation (SHG) microscopy (Figures 3B–3E). The data indicated that Impad1 regulates exocytosis and deposition of collagen proteins *in vitro* and *in vivo* to alter the ECM and drive invasion and metastasis. Last, Impad1 was also posited to alter another component of the bone and cartilage ECM, GAGs (Frederick et al., 2008; Sohaskey et al., 2008; Vissers et al., 2011). Given the role of heparanase in regulating glycoproteins, we determined the modulation of GAGs by Impad1. Using Alcian blue staining, we ascertained that GAG deposition in tumors also significantly correlated with Impad1 expression (Figure S3A). Our group has shown previously that collagen suppresses the immune microenvironment to drive metastasis and therapy resistance (Peng et al., 2020). Therefore, we ascertained the role of Impad1 in modifying the immune landscape of the TME. We performed multiparameter flow cytometry analysis for CD4+, CD8+ T cells as well as antigenpresenting cells (APCs) in syngeneic tumors with Impad1 overexpression or knockdown. Despite no consistent change in the APC populations (data not shown), Impad1 expression mediated an immunosuppressive microenvironment, as demonstrated by decreased CD4+ and CD8+ effector T cells (Figures S3B–S3G). We found that this phenotype was reversed by Impad1 knockdown, which led to a significant increase in effector T cell populations (Figures S3H–S3M). Hence, the data establish Impad1 as a key regulator of the mesenchymal cancer cell secretome, producing changes in the ECM and the immune microenvironment that are associated with a metastatic phenotype.

Impad1, a Golgi-resident protein, alters Golgi morphology and vesicular trafficking

Given that Impad1 has been established as a Golgi-resident protein (Bajaj et al., 2020; Frederick et al., 2008; Vissers et al., 2011), we investigated its role in controlling Golgi dynamics. First, we assessed the localization of Impad1 to the specific Golgi compartment. Co-staining of Impad1 with a *cis*-Golgi marker (GM130) or a *trans*-Golgi marker (Golgin97) and performing co-localization analysis (the COLOC2 analysis in ImageJ) revealed that Impad1 resides in the *cis* and *trans* Golgi compartments (Figures S4A–S4C). This indicated the spatially dynamic role of Impad1 as it shuttles between the compartments during vesicular trafficking.

Zeb1-mediated EMT drives changes in Golgi dynamics, which affects the secretome (Tan et al., 2017). However, the regulators of the EMT-driven Golgi changes are not well defined. Hence, we determined whether Impad1 orchestrates the EMT-coordinated alterations in Golgi morphology. We probed for the Golgi using GM130 and Golgin97 upon Impad1 overexpression in epithelial cells and Impad1 knockdown in mesenchymal cells. Impad1 expression produced an organized and stacked Golgi in murine 393P and 344SQ as well as in human HCC827 cells, as shown by fewer and larger individual Golgi fragments (Figures 4A–4C and S4D–S4H). Despite no change in expression of the Golgi proteins GM130 and Golgin97 (Figure S4N), Impad1 upregulation also increased the fluorescence staining intensity of the organelle (Figures 4D and S4E–S4G). Conversely, Impad1 was necessary to maintain Golgi integrity, where loss of the protein caused organelle fragmentation, as demonstrated by scattered, smaller, and more Golgi elements (Figures 4E–4H and S4I). We also confirmed this phenotype in other murine KP NSCLC models: 344P and 344LN with Impad1 knockdown (Figures S4J and S4K). As described previously (Lowe et al., 2000; Tan et al., 2017), we used GM130 fluorescence as a readout for Golgi fragmentation *in vivo*. Loss of Impad1 also disrupted the organelle in syngeneic tumors (Figure S4L). Another aspect of the Golgi that is altered during EMT is vesicular trafficking, which leads to enhanced and polarized exocytosis of factors that can modify the TME and drive metastasis (Tan et al., 2017). To determine whether Impad1 is also responsible for the EMT-enhanced vesicular trafficking, we performed vesicular stomatitis virus G (VSV-G) trafficking assays on Impad1 overexpressing and knockdown murine and human cells (Figures 4I, 4J, and S4M). Impad1 was necessary and sufficient to promote anterograde trafficking to the plasma membrane in lung cancer cells. These data demonstrate that Impad1, similar to phosphatidylinositol-4-phosphate (Tokuda et al., 2014), is a functional link between EMT, changes in Golgi secretory dynamics, and the altered metastatic cell secretome.

Impad1 interacts with another trafficking protein, Syt11

To understand how Impad1 regulates Golgi functions, we identified the interactome of the protein by using IP-MS in the 393P Impad1-FLAG-overexpressing cells. Using anti-FLAG beads, we immunoprecipitated Impad1 and performed MS to detect the interacting partners. Of the 43 significant hits ($p < 0.05$) upregulated in Impad1-overexpressing cells, we identified various proteins that are usually exocytosed and function in the extracellular space, such as apolipoproteins and the complement pathway factors (Figures 5A and S5A; Table S2). However, to identify the intracellular machinery working with Impad1 to regulate Golgi function, we investigated the two hits annotated to be associated with the Golgi, Syt11

and ADP-ribosylation factor 5 (Arf5). Using coIP, we first corroborated the interaction between Impad1 and Syt11 or Arf5 individually. Syt11 and Arf5 were validated as Impad1 interaction partners upon anti-FLAG IP in 393P Impad1FLAG-overexpressing cells (Figures 5B and S5B). However, their expression was not dependent on Impad1 levels (Figure S5C). Conversely, Syt11 pull-down in Impad1-overexpressing or Syt11 knockdown cells showed interaction with Impad1 (Figures 5C, 5D, and S5D), which was decreased upon Syt11 repression. However, Syt11 did not show any association with Arf5 (Figure S5E), indicating that Impad1 forms separate bipartite complexes with the two proteins. We also verified the interaction under endogenous conditions using wild-type KP cells distinguished by their EMT status (531LN3 and 344SQ, mesenchymal; 393P, epithelial) (Figure S5F). Last, using 393P KP cells, we showed that Syt11 colocalizes with the Golgi marker GM130 (Figure S5G). The control and Syt11 knockdown cells demonstrated that Syt11 also co-localizes with Impad1, which we confirmed to be a Golgi-resident protein (Figure S5H). There is a decrease in the degree of co-localization between Impad1 and Syt11 upon Syt11 knockdown.

As part of the Synaptotagmin family, Syt11 meditates Ca^{2+}independent vesicle docking and fusion to drive trafficking (Mikoshiba et al., 1999). Previous studies have demonstrated that Syt11 plays a critical role in dopamine release by regulating late endocytosis and the vesicle recycling process (Shimojo et al., 2019). It has also been shown to regulate lysosomal exocytosis and cytokine release primarily in neural cells (Arango Duque et al., 2013, Du et al., 2017, Wang et al., 2016, Bento et al., 2016). In the context of cancer, Syt11 is necessary for gastric cancer tumorigenesis and liver metastasis by activating the JNK pathway (Kim et al., 2022). However, the role of Syt11 in mediating Golgi exocytosis and promoting lung cancer metastasis has not been studied. Moving forward, we focused on the Impad1-Syt11 epistatic pathway and its function in modulating exocytosis for the following reasons. (1) In parallel to the *in vitro* screen that first identified Impad1 for its role in promoting lung cancer invasion, we also performed an *in vivo* gain-of-function screen for drivers of metastasis (Kundu et al., 2018; Grzeskowiak et al., 2018). In that previously published *in vivo* screen, Syt11 was identified as an independent driver of NSCLC metastasis based on a stringent cutoff that identified biologically relevant candidates (Figure S5I). Overexpression of Syt11 in 393P, 344SQ, and HCC827 cells enhanced the invasion capability of these cells, validating that it is sufficient to drive lung cancer invasion (Figures S5J–S5M). (2) Similar to Impad1, Syt11 positively correlated with the EMT gene signature and was upregulated by exposure to TGF-b1 in human and murine lung cancer cell lines and tumors (Figures 5E, 5F, and S5N–S5R). This indicated that Impad1 and Syt11 are abundant in mesenchymal cells and may be acting synergistically to alter Golgi dynamics. However, no correlation was observed between Impad1 and Syt11 expression in NSCLC tumor datasets (Figure S5S). (3) Last, Arf5, the other interaction protein identified from the IP-MS, helps maintain Golgi integrity upon treatment with drugs that enhance Golgi fragmentation (Ignashkova et al., 2017). We demonstrated that the Impad1-Arf5 interaction was necessary for Impad1-mediated Golgi organization and invasion (Figures S6A–S6C). However, loss of Arf5 did not have any significant effect on secretome-mediated invasion driven by Impad1 (Figures S6D and S6E). Thus, going forward, we specifically studied

the epistatic pathway involving Impad1 and the trafficking protein Syt11 in regulating exocytosis and the cancer cell secretome.

Syt11 is necessary to drive Impad1-mediated exocytosis, invasion, and metastasis in lung cancer

We first showed that Syt11, like Impad1, is a membrane protein by using a cell fractionation assay (Figure S6F). To investigate the role of Syt11 in altering Impad1-regulated Golgi dynamics, we performed the previously described Golgi morphology and VSV-G vesicular trafficking assays. To study the epistatic pathway, we used models with transient Syt11 knockdown upon inducible or constitutive exogenous Impad1 overexpression in 393P or HCC827 cells, respectively. We also used the stable Syt11 knockdown 344SQ cell line (Figure S5D), which has high basal endogenous Impad1 levels (Figures 1A, 1B, and S1B). Although loss of Syt11 did not affect the ability of Impad1 to maintain Golgi morphology (Figures S6G–S6I), Impad1-modulated vesicular trafficking was significantly hampered upon suppression of Syt11 (Figures 6A and S6J–S6L). Thus, we concluded that Syt11 is required for Impad1-regulated vesicular trafficking in lung cancer cells. Next we studied whether this loss in trafficking has functional relevance in inhibiting cancer cell invasion. Using the Boyden chamber invasion assay, we showed that Impad1-mediated invasion was disrupted upon transient or stable depletion of Syt11 in 344SQ, 393P, and HCC827 cells (Figures 6B–6D and S6M–S6P). Subsequently, we performed a secretome-mediated invasion assay, which evaluates the ability of cancer cells to secrete invasive components (Bajaj et al., 2020). To do this, we seeded the non-invasive 393P KP cells in invasion chambers and replenished them with CM collected from 344SQ scramble control or shSyt11 cells. The invasiveness of the secretome of 344SQ cells was significantly repressed upon stable loss of Syt11 (Figure 6E). We confirmed these changes by probing for MMP1 and MMP2 in the same CM. The heightened secretion of MMPs that was observed upon enhanced basal Impad1 levels in 344SQ cells was lost with Syt11 knockdown, as quantified by densitometric analysis using ImageJ (Figures 6F and S6Q). This phenotype was also confirmed in cells with exogenous Impad1 overexpression and transient Syt11 knockdown (Figures S6R–S6T). We subcutaneously implanted the 344SQ shSyt11 cells into mice and investigated the changes in ECM and metastasis. Similar to Impad1, loss of Syt11 did not change primary tumor volumes but decreased distant lung metastatic nodules (Figures 6G, S6U, and S6V) along with collagen deposition in tumors (Figures 6H and S6V). These data demonstrate that Syt11 is necessary for Impad1-mediated vesicular trafficking from the Golgi, which promotes secretion of invasive components that alter the ECM and TME to drive lung cancer invasion and metastasis.

DISCUSSION

Metastasis causes 90% of cancer-related deaths, and therapies targeting the process may help reduce this mortality (Fidler, 2003). However, this requires a deeper understanding of the underlying processes regulating the metastatic cascade. EMT, and enhanced Golgi kinetics during EMT, are key features of this cascade, but the relationship between these processes and their effects on metastasis is understudied. Tan et al. (2020) ascertained that a Golgi protein, PI4KIIIβ, was genomically amplified in lung cancer and responsible for secretion

of pro-survival factors such as semaphorin-3C (SEMA3C), lysyl hydroxylase-3 (PLOD3), tissue inhibitor of metalloproteinase-1 (TIMP1), and so forth. However, not enough has been determined to identify the global changes in the secretome of mesenchymal lung cancer cells. Little is known about whether Golgi-resident proteins such as Impad1 can drive these changes in the secretome. The LC-MS/MS data here demonstrate that basal mesenchymal lung cancer cells have a distinct secretome signature. They secreted factors such as Cohesin SA-1 (Stag), Advillin (Avil), fibroblast growth factor 21 (Fgf21), Matrilin-3 (Matn3), and insulin growth factor 2 (Igf2b), which are known drivers and prognostic markers for various cancers. The high degree of overlap between the secretome components of mesenchymal cells and Impad1-expressing cells (Figure 3A; Table S1) suggested that Impad1 might play a central role in EMT-mediated exocytosis in cancer.

We further established that Impad1 regulates the secretome by altering Golgi dynamics; more specifically, the functional morphology and vesicular trafficking. However, there are other Golgi functions that can also regulate the cell secretome (Pinho and Reis, 2015), which were unexplored and are beyond the scope of this paper. One such process is protein post-translational modification (PTM), such as glycosylation and sulfation, that occurs in the Golgi. Impad1 has been shown to regulate sulfated GAGs in the bone and cartilage ECM (Frederick et al., 2008; Sohaskey et al., 2008; Vissers et al., 2011). We also determined that GAG deposition is dependent on Impad1 levels in lung cancer tumors (Figure S3A). Thus, investigating the PTMs modulated by Impad1 at the Golgi could give us a deeper understanding of the glycobiology of lung cancer cells undergoing EMT. Another process that more closely relates to vesicular trafficking is endosomal recycling. Syt11, an Impad1 interaction protein, regulates endosomes to recycle dopamine at the plasma membrane for synaptic plasticity (Shimojo et al., 2019). Our data show that the Impad1-Syt11 epistatic pathway is necessary for vesicular trafficking (Figures 6A and S6J–S6L), but loss of Syt11 has no role in Impad1-mediated alterations of the Golgi architecture (Figures S6G–S6I). Thus, respective Golgi protein interactions can have specific effects on Golgi dynamics. To iterate this point, we also elucidated that Impad1 interacts with Arf5 to maintain Golgi integrity and drive invasion (Figures S6A and S6B). Surprisingly, this interaction was not necessary for promoting secretion and secretome-mediated invasion (Figure S6C). Hence, our data also indicate that Impad1 might alter Golgi dynamics and drive lung cancer invasion independent of changes in the secretome.

We demonstrated that Impad1, the topmost hit of our previously published invasion screen (Bajaj et al., 2020), is a direct target of miR-200 and miR~96 that is de-repressed upon loss of these epithelial miRNAs during EMT. EMT is a key regulator of Golgi dynamics, which contribute to the altered cancer cell secretome. However, the epistatic pathway that connects EMT, Golgi function and secretion, and metastasis remains unclear. We determined that Impad1 regulates Golgi morphology and vesicular trafficking to enhance cellular exocytosis, modifying the TME to drive malignancy. Impad1 and Syt11 are part of an epistatic pathway that determines vesicular trafficking and exocytosis of invasive components during lung cancer progression. Thus, we identified Impad1 as an important link connecting EMT, Golgi trafficking, secretome changes, and metastasis (Figure 7). We also demonstrated that repressing Impad1 or Syt11 can reverse this phenotype, leading to altered ECM and decreased exocytosis and invasion. This work gives us further insight into how Golgi

functions are regulated by a Golgi protein, Impad1, that eventually alters the TME and promotes lung cancer metastasis. It also helps us identify possible targets that can be used to regulate Golgi-mediated exocytosis to inhibit invasion and metastasis.

Limitations of the study

One of the key technical limitations of our work is the incomplete knowledge of the Impad1 protein. Given the lack of understanding about its potential interacting domain(s), it is difficult to conclusively determine how it interacts with the other proteins identified here, Syt11 and Arf5. Another technical limitation we faced was that tagging Impad1 with a fluorescence protein rendered it dysfunctional and led to protein degradation. Hence, our study relied on analysis of static confocal images instead of live-cell imaging to study Impad1-mediated trafficking. LC-MS/MS was performed on the CM collected from the cells. However, our work did not distinguish between the extracellular vesicle-bound proteins and the “free” proteins. Studying this could further elucidate the secretome regulated by Impad1. Conceptually, there were also limitations in the literature exploring trafficking-independent functions of Impad1 and Syt11. Syt11, for example, has been shown recently to drive gastric cancer and liver metastasis by altering the JNK pathway (Kim et al., 2022). Further research into Syt11 would reveal whether it acts as a link to connect trafficking with signalling pathways involved in cancer. These potential roles of the proteins, along with a better understanding of their dynamic protein interactions, will provide fruitful ground for further investigations.

STAR★METHODS

RESOURCE AVAILABILITY

Lead contact—Further information and requests for resources and reagents should be directed to and will be fulfilled by the lead contact, Don L. Gibbons (dlgibbon@mdanderson.org).

Materials availability—All unique reagents generated in this study are available upon request from the lead contact.

Data and code availability

- Data generated in this study are available in Tables S1 and S2.
- This paper does not report original code.
- Any additional information required to re-analyze the data reported in this paper is available from the lead contact upon request.

EXPERIMENTAL MODEL AND SUBJECT DETAILS

Animal models—The latent $Kras^{G12D}$ mutation in combination with the $Tp53^{R172H}$ produces metastatic lung adenocarcinoma (denoted as KP), as previously described (Gibbons et al., 2009b, 2014; Zheng et al., 2007). We additionally used conditional miR-200 or miR~96 floxed mice and crossed them with the KRAS or KP mice to produce $KRAS^{G12D/+}$;miR-200c$^{fl/fl}$ (KM), $KRAS^{G12D/+}$;$p53^{R172H}$;miR-200c$^{fl/fl}$ (KPM200),

and KRAS$^{G12D/+}$;miR~96$^{fl/fl}$ (KM96) animal models to study EMT (Kundu et al., 2022; Peng et al., 2019). The mice we used were 9 males and 5 females at 14.7 months.

Cell lines—For all tissue culture assays, cells were plated in 10% FBS + RPMI-1640 (complete media) in 5% CO2 at 37°C. Inducible cells were doxycycline-induced (2uM) for 24 h before experiments unless specified. Cell lines were generated and authenticated in our lab and regularly tested for mycoplasma (Gibbons et al., 2009a). H441, H358, HCC827, H157, H1299, A549 human lung, and NMuMG murine breast cancer cells were procured from ATCC. Our group developed cell lines from the primary tumors as well as the various metastatic lesions of the KP mice, which grow as syngeneic tumors upon reimplantation into immune competent mice (129/Sv) – KP cell panel (Gibbons et al., 2009a). Cell lines were also derived from the KPM200 mice (KPM200 cells), which were used to compare to the KRAS- or KP-derived cell lines.

METHOD DETAILS

Tissue culture and transfections—siRNA transfection was performed with RNAiMAX Lipofectamine (Life Technologies, #13778) as per manufacturer protocol. For mouse Syt11, siRNA (Dharmacon, #SO-2959152G) transfection was performed for ~40 h at a final concentration of 30nM in 393P cells. In 344SQ cells, two rounds of siSyt11 transfections were carried out for ~72 h at a final concentration of 30nM. For mouse Arf5, siRNA (Dharmacon, #SO-2952843G) transfection was performed for ~40 h at a final concentration of 50nM in 393P cells. Non-targeting pool was used as negative control (Dharmacon, #SO-2968428G). siRNA sequences in Table S3.

qPCR and Western blot—Cells were lysed in TRIzol (Ambion) and RNA was isolated by using Direct-zol RNA miniprep plus kit (Zymo Research, #R2072). RT-PCR was performed with primers specific for cDNAs (Key Resources Table and Table S3) and SYBR Green PCR Master Mix (Life Technologies). qPCR analyses were normalized to control gene L32.

Cells were lysed in RIPA buffer (Cell Signaling Technologies, USA). Protein lysates were run on 10% Bis-Acrylamide gels and transferred to nitrocellulose membranes. 5% milk in TBST (10 mM Tris, 100 mM NaCl, and 0.1% Tween 20) was used as blocking buffer. Primary antibody was O/N at 4°C and secondary antibodies were incubated for 1hour and RT in 2.5% milk/TBS-T. Blots were finally visualized using an ECL detection system (LF-Q0101, 27B09). β-actin was used as loading control. Densitometric analysis on blots for quantifying MMP levels were performed using ImageJ. Antibody details in Key Resources Table.

Immunohistochemistry—Formalin-fixed, paraffin-embedded tissues were cut into 4μm sections. The sections were de-thawed in Xylene and rehydrated in sequentially diluted ethanol baths. Citric acid (s1399, Dako, USA) was used for antigen retrieval and 3% H_2O_2 was used to block endogenous peroxidase activity. Sections were then incubated O/N at 4°C with primary antibody and 1 h at RT with secondary antibody. Immunohistochemistry was

carried out using Streptavidin (Life technologies #SNN1004), Envision + System (Dako), and HRPDAB (Dako) colorimetric detection. Antibody details in Key Resources Table.

3'UTR luciferase reporter assay—The 3'UTR of murine Impad1 was PCR-amplified from the 344SQ WT genomic DNA and cloned downstream of Firefly Luciferin gene in the pMirGLO (Promega, #E1330) plasmid with the restriction sites XhoI-Sbf1. The Renilla Luciferin gene in the pMirGLO plasmid was used as an internal control. The QuikChange Lightning MULTI Site-Directed Mutagenesis Kit (Agilent, Santa Clara, CA, USA) was used to make mutations in the miR-200 or miR~96/183 binding sites in Impad1 3' UTR. 393P WT cells were plated in 24-well plates the previous day so that they were 60% confluent at time of transfection. For 3' UTR luciferase reporter assays, cells were co-transfected with 1μg pMirGLO plasmid (Promega, #E1330) and 60 pmol miR-200a/b/c or miR-96/183 mimics (Ambion by Life Technologies, #4464066). Negative mimics were used as the negative control. Transfection was performed by using Lipofectamine 2000 (Life Technologies, #11668019). Assays were carried out as per manufacturer instructions with Dual-Luciferase Reporter Assay kit (Promega, #1910). Relative luciferin signal was normalized to signal from the negative mimic controls. Primers used to clone and sequence Impad1 3'UTR, and miRNA mimic sequence in Table S3.

Liquid chromatography-mass spectrometry—Cells were grown in 15-cm plates in serum-free media and incubated with doxycycline for 48 h. Conditioned media was filtered and concentrated (Millipore Amicon, Cat# UFC901024) and sent for mass spectrometry analysis to proteomics core at UTMB. Samples were made with 5% SDS, 50 mM TEAB, pH 7.55, then reduced in 20 mM TCEP solution (Thermo Fisher Scientific, #77720) at 65°C for 30 min. The sample was treated with 0.5 M iodoacetamide acid at RT for 20 min. Next, 12% phosphoric acid was added to the solution, followed by binding buffer (90% methanol, 100 mM TEAB, final pH 7.1). The solution was spun using S-Trap spin columns (protifi.com) at 4,000xg for 30s, then washed with binding buffer (90% methanol, 100mM TEAB, pH = 7.55) and treated with Trypsin (50 mM TEAB, pH 8) at 37°C for 4 h. Peptides were eluted with 50 mM TEAB, followed by 0.2% formic acid, and finally 50% acetonitrile, 0.2% formic acid. The solution was then dried in a speed vac and resuspended in 2% acetonitrile, 0.1% formic acid, 97.9% water.

Nano LC MS/MS analysis: Peptide mixtures were analyzed by nanoflow liquid chromatography-tandem mass spectrometry (nanoLC-MS/MS) using a nano-LC chromatography system (UltiMate 3000 RSLCnano, Dionex), coupled on-line to a Thermo Orbitrap Eclipse mass spectrometer (Thermo Fisher Scientific, San Jose, CA) through a nanospray ion source coupled with a FAIMS Pro device (Thermo Fisher Scientific) with Instrument Control Software version 3.4. FAIMS separations were performed at Standard Resolution with the following settings: inner and outer electrode temperature = 100°C; FAIMS gas flow = 0 L/min, Compensation Voltages (CV): −45, −60 and −70 with 2 s cycle times per CV. A trap-and-elute method was used: The trap column is a C18 PepMap100 (300um X 5mm, 5um particle size) from ThermoScientific. The analytical columns is an Aurora (75um X 25 cm, 1.6 μm) from (Ionopticks). After equilibrating the column in 98% solvent A (0.1% formic acid in water) and 2% solvent B (0.1% formic acid in

acetonitrile (ACN)), the samples (2 μL in solvent A) were injected onto the trap column and subsequently eluted (400 nL/min) by gradient elution onto the C18 column as follows: isocratic at 2% B, 0–5 min; 2%–4% 5–6 min, 4%–25% B, 6–70 min; 25%–38% B, 70–97 min; 38%–90% B, 97–100 min; isocratic at 90% B, 101102 min; 90%–5%, 102.5–103 min; 5% 102.5–103min; 90%–5% 104–105 min; and isocratic at 2% B, till 120 min.

Database searching: Tandem mass spectra were extracted and charge state deconvoluted by Proteome Discoverer (Thermo Fisher, version 2.5). Deiso-toping is not performed. All MS/MS spectra were searched against a Uniprot Mus Musculus and common contaminant database (version 03–29-2016) using Sequest. Searches were performed with a parent ion tolerance of 5 ppm and a fragment ion tolerance of 0.60 Da. Trypsin is specified as the enzyme, allowing for two missed cleavages. Fixed modification of carbamidomethyl (C) and variable modifications of oxidation (M) and deamidation were specified in Sequest.

Masson's trichrome staining—Subcutaneous (SQ) tumor tissues that were stained for collagen as per manufacturer's protocol (Sigma-Aldrich, #HT15). Tissues were imaged at 20× magnification with 5 representative images per tumor. Quantification was by ImageJ analysis.

Alcian blue staining—Subcutaneous tumors were stained for sulfated GAGs as per manufacturer's protocol (Abcam, #ab150662). Imaging and quantification were similar to Masson's trichrome staining.

Second harmonic generation microscopy—Subcutaneous tumor tissues that were stained by H&E were visualized using a Zeiss LSM 7 MP Multiphoton Microscope at an excitation wavelength of 800 nm and collagen fiber signals were visualized at 380–430 nm using bandpass filters.

Flow cytometry—Flow cytometry staining, gating, and analysis were performed as previously described (Peng et al., 2021). Briefly, subcutaneous tumors were first mechanically dissociated and then enzymatically digested using digestion media [RPMI-1640 containing 2 U/mL dispase II (Roche) and 0.5% w/v collagenase type I (Thermo Fisher)] at 37°C for 45 min. Tumor cell suspensions were then filtered through a 70 μm Falcon Nylon cell strainer (Fisher Scientific). Like tumors, spleens were mechanically dissociated but filtered through a 40 μm Falcon Nylon cell strainer. Cells were centrifuged at 800xg for 5 min and resuspended in RBC lysis buffer (Biolegend) for 2 min at RT, after which lysis was inhibited using complete media. Cells were finally centrifuged and resuspended in FACS buffer (PBS + 2% FBS + 1 mM EDTA). 2×10^6 cells per sample were stained with fluorescently-labeled antibodies. For intracellular staining, cells were fixed in 1% PFA and permeabilized in permeabilization buffer (BD Biosciences) for 30 mins at RT. Cells were then stained with respective fluorescently-labeled antibodies. FlowJo 10.8.1 was used to analyze FACS data. Antibody details in Key Resources Table.

Co-immunofluorescence staining experiments

Impad1 and GM130: Cells were grown on 8-well chambered glass slides (Nunc, Naperville, IL) coated with poly-L-lysine and fixed in 4% paraformaldehyde with 50uM CaCl2 in PBS for 20 min at 37°C, followed by permeabilization with 0.1% Triton X-100 for 10 min at RT. Cells were then blocked with 5% goat serum in PBS for 1 h at RT and then incubated with primary antibody human Impad1 O/N at 4°C. Cells were sequentially incubated with fluorophore-conjugated secondary antibodies. First, Alexa 546-conjugated anti-mouse and then GM130. Each of the secondary antibodies were incubated for 1 h at RT and then counterstained with DAPI by mounting with VECTASHIELD Hard-Set Mounting Medium (Vector Laboratories, Burlingame, CA). Cells were imaged by confocal microscopy and analyzed for their Golgi area and Golgi fragments. Antibody details in Key Resources Table. Impad1 and Golgin97. Primary antibodies were human Impad1 and mouse Golgin97 O/N at 4°C. Fluorophore-conjugated secondary antibodies Alexa 546-conjugated anti-mouse and Alexia 488-conjugated anti-rabbit were incubated for 1 h at RT. Antibody details in Key Resources Table. Impad1 and Syt11. Primary antibodies were Impad1 and Syt11 O/N at 4°C. Fluorophore-conjugated secondary antibodies Alexa 546-conjugated anti-sheep and Alexia 488-conjugated anti-rabbit were incubated for 1 h at RT. Antibody details in Key Resources Table.

Immunofluorescence staining for GM130 in tumors sections—Followed the protocol as described in (Tan et al., 2017; Robertson and Isacke, 2011). Briefly, paraffin-embedded tissues were de-paraffinized and dehydrated. Citric acid (s1399, Dako, USA) was used for antigen retrieval. Sections were blocked and then incubated with fluorophore-conjugated GM130 antibody for 1 h at RT. Tissues were counterstained with DAPI and imaged by confocal microscopy using Zstacks. Golgi fragmentation was quantified by normalized fluorescence intensity. Antibody details in Key Resources Table.

Quantification of Golgi area and Golgi fragment size and number—All analyses were done by using ImageJ (NIH; https://imagej.nih.gov/ij/), following the previously described protocol (Tan et al., 2017). Briefly, GM130-stained Golgi was quantified in volume projections with a limiting polygon. Golgi area was normalized by dividing by the nucleus area in the same cell (n = 50 cells). Cells with a well-defined Golgi and nucleus were selected randomly for quantification.

Golgi fragment size and number were determined from maximum intensity projections of deconvolved, thresholded (Otsu), and watershed-segmented 3D stacks (n = 75 cells).

VSV-G transport assay—Followed previously described protocol (Tan et al., 2017). The EGFP-VSV-G (ts045) plasmid (Addgene, #11912) was a gift from Dr. Jonathan Kurie (UT MD Anderson Cancer Center, Houston, Texas, USA). EGFP-VSV-G (ts045) was transiently transfected into cells using JetPRIME transfection reagent (Polyplus, #114–07), which were then induced with doxycycline for 24 h. Cells were then transferred to a restrictive temperature of 40°C for 20 h. They were then treated with cycloheximide (1 μM) and transferred to a permissive temperature of 32°C for 1 h. Cells were then fixed with formaldehyde (Invitrogen, #FB002) at 32°C for 10 min, blocked with 2% BSA/

PBS, the exofacial VSV-G stained with anti–VSV-G primary antibody for 1 h at RT, and stained with anti-mouse secondary antibody for 1 h at RT. Cells were counterstained with DAPI by mounting with VECTASHIELD Hard-Set Mounting Medium (Vector Laboratories, Burlingame, CA) and imaged by confocal microscopy. Fluorescence intensity was quantified for exofacial (red) and total VSV-G (green), and that ratio was plotted. A total of 20 images per group were smoothed using a median filter and thresholded (Otsu). Pixel-by-pixel ratio images were generated using the following equation: (intA – bkgA)/(intB – bkgB) × MF, where intR, intA, and intB are the intensities of the ratio image, first-channel images, and second-channel images, respectively, bkgA and bkgB are the background values of the corresponding images, and MF is an arbitrary multiplication factor. Pseudocolored images were generated by a custom gradient lookup table. For visualization purposes, the pseudocolored images were intensity-calibrated. Antibody details in Key Resources Table.

For VSV-G assay with siSyt11, transfection for both Syt11 siRNA (RNAiMAX) and VSV-G (JetPRIME) were done simultaneously. Assay was then performed as mentioned above.

Immunoprecipitation-mass spectrometry—Cells were grown on 15-cm plates and induced with doxycycline for 48 h. Agarose beads (Santa Cruz, #sc2003) were conjugated with anti-mouse IgG antibody (Santa Cruz, #sc2025) O/N at 4°C. NET-N (125mM NaCl, 50mM Tris-Hcl pH 8.0, 0.5% NP-40) buffer was used to lyse the cells and lysate was pre-cleared with agarose beads (IgG antibody for 1 h at 4°C then beads for 30 min at 4°C). For Flag IP, lysate was incubated with flag-tagged beads (Biotool, #B23101) for 2 h at 4C. Beads were then washed with 1X TBS (as per protocol) and sent for mass spectrometry analysis to the proteomics core at UTMB. Samples were prepared in 5% SDS, 50mM TEAB, pH = 7.5. The agarose beads were incubated for 30 min at 37°C, after which the supernatant was processed as described in the LC/MS section above.

Co-immunoprecipitation—Cells were grown, lysed, and pre-cleared as described above. Anti-rabbit IgG (Cell Signaling Technology, #2729) and anti-Syt11 antibody was conjugated to agarose beads. For IP, lysate was incubated with IgG, or Syt11-conjugated beads for 3 h at 4°C. Beads were washed with NET-N buffer and lysate prepared for Western blot. Antibody details in Key Resources Table.

Cell fractionation—Cell fractionation was performed using a kit as per the manufacturer's protocol (Cell signaling technologies, #9038). Fractions were analyzed by western blotting. Antibody details in Key Resources Table.

Migration and invasion assay—Transwell migration (8uM inserts, BD-Biosciences) and invasion (BD-Biosciences #354480) assays were performed for both mouse and human cells using standard protocol (Kundu et al., 2018). 50,000 cells/well were plated in Boyden chamber with serum-free media. Complete media was added to the lower chamber and cells were incubated at 37°C for 16 h. Inserts were then stained with 0.1% crystal violet and cells that did migrate or invade were imaged in five representative fields at 10× magnification. An ImageJ macro was used to quantify the number of cells and results were represented as previously described (Kundu et al., 2016). Data was plotted as number of cells migrated or invaded.

Secretome-mediated invasion assay—Syt11 siRNA knockdown in 6-well plates. Cells were then induced with doxycycline for 24 h and conditioned media was collected from siControl or siSyt11 cells. 393P WT parental cells were suspended in the conditioned media and plated in invasion Boyden chambers (BD-Biosciences #354480). 50,000 cells were used per chamber. RPMI with 20% FBS was added to the lower chamber wells and the cells were incubated for 16 h at 37°C. Inserts were stained with crystal violet and cells that invaded were quantified by using ImageJ software. Data was plotted as number of cells invaded.

Conditioned media Western blot—Western blots were performed using conditioned media from the respective cells for MMP1 and MMP2. Antibody details in Key Resources Table.

QUANTIFICATION AND STATISTICAL ANALYSIS

Experiments were all done in at least biological duplicates. Data are represented as mean of triplicates ±SD. Significance by Student's T test. p-value<0.05 - *; <0.002 - **. 3'UTR Luciferase reporter assay was done in technical replicates of 4 (Figures 2 and S2). For VSV-G assays in Figures 4 and 6, statistical outliers were removed. Detailed statistical info is in the respective figure legends.

Analysis of human cancer datasets

Correlation with EMT.: For mRNA correlation in NSCLC cell lines, previously published UTSW dataset was used (N = 118) (Mcmillan et al., 2018). For mRNA correlation in LuAd tumors, TCGA Firehose legacy dataset was used (N = 555 for dataset with mRNA only). EMT score was calculated using previously determined EMT signature (Byers et al., 2013). Correlations analysis were shown as Spearman's rank correlation with a p value < 0.05.

miRNA correlations in NSCLC cell lines, Affymetrix microRNA 4.0 samples were processed by Affymetrix Expression Console (Kundu et al., 2016). For miRNA correlations in LuAd tumors, TCGA Firehose legacy dataset was used (N = 414 for dataset with mRNA and miRNA). Correlations analysis were shown as Spearman's rank correlation with a p value < 0.05.

Correlation of IMPAD1 and ZEB1 protein levels in lung cancer patient samples, IHC was performed on NSCLC whole sections with selected cases from a tissue microarray (TMA3) with ZEB1 expression. Protocol was followed as described in immunohistochemistry section except, antigen retrieval: pH-6, at 100°C for 20 min, and primary antibody staining with IMPAD1 (1:200, Sigma, Cat# HPA009411). Signal was quantified using HALO (Indica Lab) software, and correlation analysis was shown as Spearman's rank correlation with a p value < 0.05.

Supplementary Material

Refer to Web version on PubMed Central for supplementary material.

ACKNOWLEDGMENTS

This work was supported by NIH R37CA214609, NIH 2P50CA070907-21A, CPRIT-MIRA RP160652-P3, the MD Anderson Physician-Scientist Program, and Rexanna's Foundation for Fighting Lung Cancer (to D.L.G.). R.B. was supported by a CPRIT Research Training Grant (RP170067). The work was also supported by generous philanthropic contributions to The University of Texas MD Anderson Lung Cancer Moon Shots Program. We thank the UTMDACC Department of Veterinary Medicine facility. The Flow Cytometry Lab South Campus Core facility at MD Anderson Cancer Center is supported by Cancer Center Support Grant NCI P30 CA16672. The mass spectrometry facility at UTMB is supported in part by Cancer Prevention Research Institute of Texas (CPRIT) grant RP190682.

REFERENCES

Ahn YH, Gibbons DL, Chakravarti D, Creighton CJ, Rizvi ZH, Adams HP, Pertsemlidis A, Gregory PA, Wright JA, Goodall GJ, et al. (2012). ZEB1 drives prometastatic actin cytoskeletal remodeling by downregulating miR-34a expression. J. Clin. Invest. 122, 3170–3183. [PubMed: 22850877]

Arango Duque G, Fukuda M, and Descoteaux A. (2013). Synaptotagmin Xi regulates phagocytosis and cytokine secretion in macrophages. J. Immunol. 190, 1737–1745. [PubMed: 23303671]

Bajaj R, Kundu ST, Grzeskowiak CL, Fradette JJ, Scott KL, Creighton CJ, and Gibbons DL (2020). IMPAD1 and KDELR2 drive invasion and metastasis by enhancing Golgi-mediated secretion. Oncogene 39, 5979–5994. [PubMed: 32753652]

Bajaj R, Warner AN, Fradette JF, and Gibbons DL (2022). Dance of the Golgi: understanding Golgi dynamics in cancer metastasis. Cells 11.

Bento CF, Ashkenazi A, Jimenez-Sanchez M, and Rubinsztein DC (2016). The Parkinson's disease-associated genes ATP13A2 and SYT11 regulate autophagy via a common pathway. Nat. Commun. 7, 11803. [PubMed: 27278822]

Bracken CP, Li X, Wright JA, Lawrence DM, Pillman KA, Salmanidis M, Anderson MA, Dredge BK, Gregory PA, Tsykin A, et al. (2014). Genome-wide identification of miR-200 targets reveals a regulatory network controlling cell invasion. EMBO J. 33, 2040–2056. [PubMed: 25069772]

Byers LA, Diao L, Wang J, Saintigny P, Girard L, Peyton M, Shen L, Fan Y, Giri U, Tumula PK, et al. (2013). An epithelial-mesenchymal transition gene signature predicts resistance to EGFR and PI3K inhibitors and identifies Axl as a therapeutic target for overcoming EGFR inhibitor resistance. Clin. Cancer Res. 19, 279–290. [PubMed: 23091115]

Du C, Wang Y, Zhang F, Yan S, Guan Y, Gong X, Zhang T, Cui X, Wang X, and Zhang CX (2017). Synaptotagmin-11 inhibits cytokine secretion and phagocytosis in microglia. Glia 65, 1656–1667. [PubMed: 28686317]

Eccles MR, Chatterjee A, and Rodger EJ (2017). Identifying drivers of metastasis; towards a systematic approach. Transl. Cancer Res. 6, S273–S276.

Fidler IJ (2003). The pathogenesis of cancer metastasis: the 'seed and soil' hypothesis revisited. Nat. Rev. Cancer 3, 453–458. [PubMed: 12778135]

Frederick JP, Tafari AT, Wu SM, Megosh LC, Chiou ST, Irving RP, and York JD (2008). A role for a lithium-inhibited Golgi nucleotidase in skeletal development and sulfation. Proc. Natl. Acad. Sci. USA 105, 11605–11612. [PubMed: 18695242]

Gibbons DL, Byers LA, and Kurie JM (2014). Smoking, P53 mutation, and lung cancer. Mol. Cancer Res. 12, 3–13. [PubMed: 24442106]

Gibbons DL, Lin W, Creighton CJ, Rizvi ZH, Gregory PA, Goodall GJ, Thilaganathan N, Du L, Zhang Y, Pertsemlidis A, and Kurie JM (2009a). Contextual extracellular cues promote tumor cell EMT and metastasis by regulating miR-200 family expression. Genes Dev. 23, 2140–2151. [PubMed: 19759262]

Gibbons DL, Lin W, Creighton CJ, Zheng S, Berel D, Yang Y, Raso MG, Liu DD, Wistuba I, Lozano G, and Kurie JM (2009b). Expression signatures of metastatic capacity in a genetic mouse model of lung adenocar-cinoma. PLoS One 4, E5401. [PubMed: 19404390]

Goldenring JR (2013). A central role for vesicle trafficking in epithelial neoplasia: intracellular highways to carcinogenesis. Nat. Rev. Cancer 13, 813–820. [PubMed: 24108097]

Gregory PA, Bert AG, Paterson EL, Barry SC, Tsykin A, Farshid G, Vadas MA, Khew-Goodall Y, and Goodall GJ (2008). The miR-200 family and miR-205 regulate epithelial to mesenchymal transition by targeting ZEB1 and SIP1. Nat. Cell Biol. 10, 593–601. [PubMed: 18376396]

Grzeskowiak CL, Kundu ST, Mo X, Ivanov AA, Zagorodna O, Lu H, Chapple RH, Tsang YH, Moreno D, Mosqueda M, et al. (2018). In vivo screening identifies GATAD2B as a metastasis driver in KRAS-driven lung cancer. Nat. Commun. 9, 2732. [PubMed: 30013058]

Howley BV, and Howe PH (2018). Metastasis-associated upregulation of ER-Golgi trafficking kinetics: regulation of cancer progression via the Golgi apparatus. Oncoscience 5, 142–143. [PubMed: 30035168]

Ignashkova TI, Gendarme M, Peschk K, Eggenweiler HM, Lindemann RK, and Reiling JH (2017). Cell survival and protein secretion associated with Golgi integrity in response to Golgi stress-inducing agents. Traffic 18, 530–544. [PubMed: 28485883]

Kalluri R, and Weinberg RA (2009). The basics of epithelial-mesenchymal transition. J. Clin. Invest. 119, 1420–1428. [PubMed: 19487818]

Kim BK, Kim DM, Park H, Kim SK, Hwang MA, Lee J, Kang MJ, Byun JE, Im JY, Kang M, et al. (2022). Synaptotagmin 11 scaffolds MKK7-JNK signaling process to promote stem-like molecular subtype gastric cancer oncogenesis. J. Exp. Clin. Cancer Res. 41, 212. [PubMed: 35768842]

Kundu ST, Byers LA, Peng DH, Roybal JD, Diao L, Wang J, Tong P, Creighton CJ, and Gibbons DL (2016). The miR-200 family and the miR183~96~182 cluster target Foxf2 to inhibit invasion and metastasis in lung cancers. Oncogene 35, 173–186. [PubMed: 25798833]

Kundu ST, Grzeskowiak CL, Fradette JJ, Gibson LA, Rodriguez LB, Creighton CJ, Scott KL, and Gibbons DL (2018). TMEM106B drives lung cancer metastasis by inducing TFEB-dependent lysosome synthesis and secretion of cathepsins. Nat. Commun. 9, 2731. [PubMed: 30013069]

Kundu ST, Rodriguez BL, Gibson LA, Warner AN, Perez MG, Bajaj R, Fradette JJ, Class CA, Solis LM, Rojas Alvarez FR, et al. (2022). The microRNA-183/96/182 cluster inhibits lung cancer progression and metastasis by inducing an interleukin-2-mediated antitumor CD8(+) cytotoxic T-cell response. Genes Dev. 36, 582–600. [PubMed: 35654454]

Larsen JE, Nathan V, Osborne JK, Farrow RK, Deb D, Sullivan JP, Dospoy PD, Augustyn A, Hight SK, Sato M, et al. (2016). ZEB1 drives epithelial-to-mesenchymal transition in lung cancer. J. Clin. Invest. 126, 3219–3235. [PubMed: 27500490]

Lowe M, Gonatas NK, and Warren G. (2000). The mitotic phosphorylation cycle of the cis-Golgi matrix protein GM130. J. Cell Biol. 149, 341–356. [PubMed: 10769027]

Mcmillan EA, Ryu MJ, Diep CH, Mendiratta S, Clemenceau JR, Vaden RM, Kim JH, Motoyaji T, Covington KR, Peyton M, et al. (2018). Chemistry-first approach for nomination of personalized treatment in lung cancer. Cell 173, 864–878.e9. [PubMed: 29681454]

Mikoshiba K, Fukuda M, Ibata K, Kabayama H, and Mizutani A. (1999). Role of synaptotagmin, A Ca2+ and inositol polyphosphate binding protein, in neurotransmitter release and neurite outgrowth. Chem. Phys. Lipids 98, 59–67. [PubMed: 10358928]

Mughees M, Chugh H, and Wajid S. (2020). Vesicular trafficking-related proteins as the potential therapeutic target for breast cancer. Protoplasma 257, 345–352. [PubMed: 31828433]

Nieto MA, Huang RY, Jackson RA, and Thiery JP (2016). EMT: 2016. Cell 166, 21–45. [PubMed: 27368099]

Ojha R, and Amaravadi RK (2017). Targeting the unfolded protein response in cancer. Pharmacol. Res. 120, 258–266. [PubMed: 28396092]

Padhye A, Konen JM, Rodriguez BL, Fradette JJ, Ochieng JK, Diao L, Wang J, Lu W, Solis LS, Batra H, et al. (2021). Targeting CDK4 overcomes EMT-mediated tumor heterogeneity and therapeutic resistance in KRAS-mutant lung cancer. JCI Insight 6.

Peng DH, Kundu ST, Fradette JJ, Diao L, Tong P, Byers LA, Wang J, Canales JR, Villalobos PA, Mino B, et al. (2019). ZEB1 suppression sensitizes KRAS mutant cancers to MEK inhibition by an IL17RD-dependent mechanism. Sci. Transl. Med. 11.

Peng DH, Rodriguez BL, Diao L, Chen L, Wang J, Byers LA, Wei Y, Chapman HA, Yamauchi M, Behrens C, et al. (2020). Collagen promotes anti-PD-1/PD-L1 resistance in cancer through LAIR1-dependent CD8(+) T cell exhaustion. Nat. Commun. 11, 4520. [PubMed: 32908154]

Peng DH, Rodriguez BL, Diao L, Gaudreau P-O, Padhye A, Konen JM, Ochieng JK, Class CA, Fradette JJ, Gibson L, et al. (2021). TH17 cells contribute to combination MEK inhibitor and anti-PD-L1 therapy resistance in KRAS/P53 mutant lung cancers. Nat. Commun. 12, 2606. [PubMed: 33972557]

Peng DH, Ungewiss C, Tong P, Byers LA, Wang J, Canales JR, Villalobos PA, Uraoka N, Mino B, Behrens C, et al. (2017). ZEB1 induces LOXL2-mediated collagen stabilization and deposition in the extracellular matrix to drive lung cancer invasion and metastasis. Oncogene 36, 1925–1938. [PubMed: 27694892]

Pinho SS, and Reis CA (2015). Glycosylation in cancer: mechanisms and clinical implications. Nat. Rev. Cancer 15, 540–555. [PubMed: 26289314]

Reka AK, Chen G, Jones RC, Amunugama R, Kim S, Karnovsky A, Standiford TJ, Beer DG, Omenn GS, and Keshamouni VG (2014). Epithelial-mesenchymal transition-associated secretory phenotype predicts survival in lung cancer patients. Carcinogenesis 35, 1292–1300. [PubMed: 24510113]

Robertson D, and Isacke CM (2011). Multiple immunofluorescence labeling of formalin-fixed paraffin-embedded tissue. Methods Mol. Biol. 724, 69–77. [PubMed: 21370006]

Shimojo M, Madara J, Pankow S, Liu X, Yates J 3rd, Südhof TC, and Maximov A. (2019). Synaptotagmin-11 mediates a vesicle trafficking pathway that is essential for development and synaptic plasticity. Genes Dev. 33, 365–376. [PubMed: 30808661]

Siegel RL, Miller KD, Fuchs HE, and Jemal A. (2021). Cancer statistics, 2021. CA Cancer J. Clin. 71, 7–33. [PubMed: 33433946]

Sohaskey ML, Yu J, Diaz MA, Plaas AH, and Harland RM (2008). JAWS coordinates chondrogenesis and synovial joint positioning. Development 135, 2215–2220. [PubMed: 18539921]

Steeg PS, and Theodorescu D. (2008). Metastasis: a therapeutic target for cancer. Nat. Clin. Pract. Oncol. 5, 206–219. [PubMed: 18253104]

Tan X, Banerjee P, Guo HF, Ireland S, Pankova D, Ahn YH, Nikolaidis IM, Liu X, Zhao Y, Xue Y, et al. (2017). Epithelial-to-mesenchymal transition drives a pro-metastatic Golgi compaction process through scaffolding protein PAQR11. J. Clin. Invest. 127, 117–131. [PubMed: 27869652]

Tan X, Banerjee P, Pham EA, Rutaganira FUN, Basu K, Bota-Rabassedas N, Guo HF, Grzeskowiak CL, Liu X, Yu J, et al. (2020). PI4KIIIβ is a therapeutic target in chromosome 1q-amplified lung adenocarcinoma. Sci. Transl. Med. 12.

Thiery JP, Acloque H, Huang RY, and Nieto MA (2009). Epithelialmesenchymal transitions in development and disease. Cell 139, 871–890. [PubMed: 19945376]

Tokuda E, Itoh T, Hasegawa J, Ijuin T, Takeuchi Y, Irino Y, Fukumoto M, and Takenawa T. (2014). Phosphatidylinositol 4-phosphate in the Golgi apparatus regulates cell-cell adhesion and invasive cell migration in human breast cancer. Cancer Res. 74, 3054–3066. [PubMed: 24706697]

Ungewiss C, Rizvi ZH, Roybal JD, Peng DH, Gold KA, Shin D-H, Creighton CJ, and Gibbons DL (2016). The microRNA-200/Zeb1 Axis regulates ECM-dependent B1-integrin/FAK signaling, cancer cell invasion and metastasis through CRKL. Sci. Rep. 6, 18652. [PubMed: 26728244]

Vissers LE, Lausch E, Unger S, Campos-Xavier AB, Gilissen C, Rossi A, Del Rosario M, Venselaar H, Knoll U, Nampoothiri S, et al. (2011). Chondrodysplasia and abnormal joint development associated with mutations in IMPAD1, encoding the Golgi-resident nucleotide phosphatase, gPAPP. Am. J. Hum. Genet. 88, 608–615. [PubMed: 21549340]

Wang C, Wang Y, Hu M, Chai Z, Wu Q, Huang R, Han W, Zhang CX, and Zhou Z. (2016). Synaptotagmin-11 inhibits clathrin-mediated and bulk endocytosis. EMBO Rep. 17, 47–63. [PubMed: 26589353]

Zheng S, El-Naggar AK, Kim ES, Kurie JM, and Lozano G. (2007). A genetic mouse model for metastatic lung cancer with gender differences in survival. Oncogene 26, 6896–6904. [PubMed: 17486075]

Highlights

- Impad1 is a target of miR-200 and miR~96 and is de-repressed during EMT
- Impad1 regulates Golgi apparatus structure and trafficking to alter exocytosis and TME
- Syt11 is necessary for Impad1-mediated exocytosis, invasion, and metastasis
- Inhibiting Impad1 or Syt11 represses lung cancer invasion and metastasis

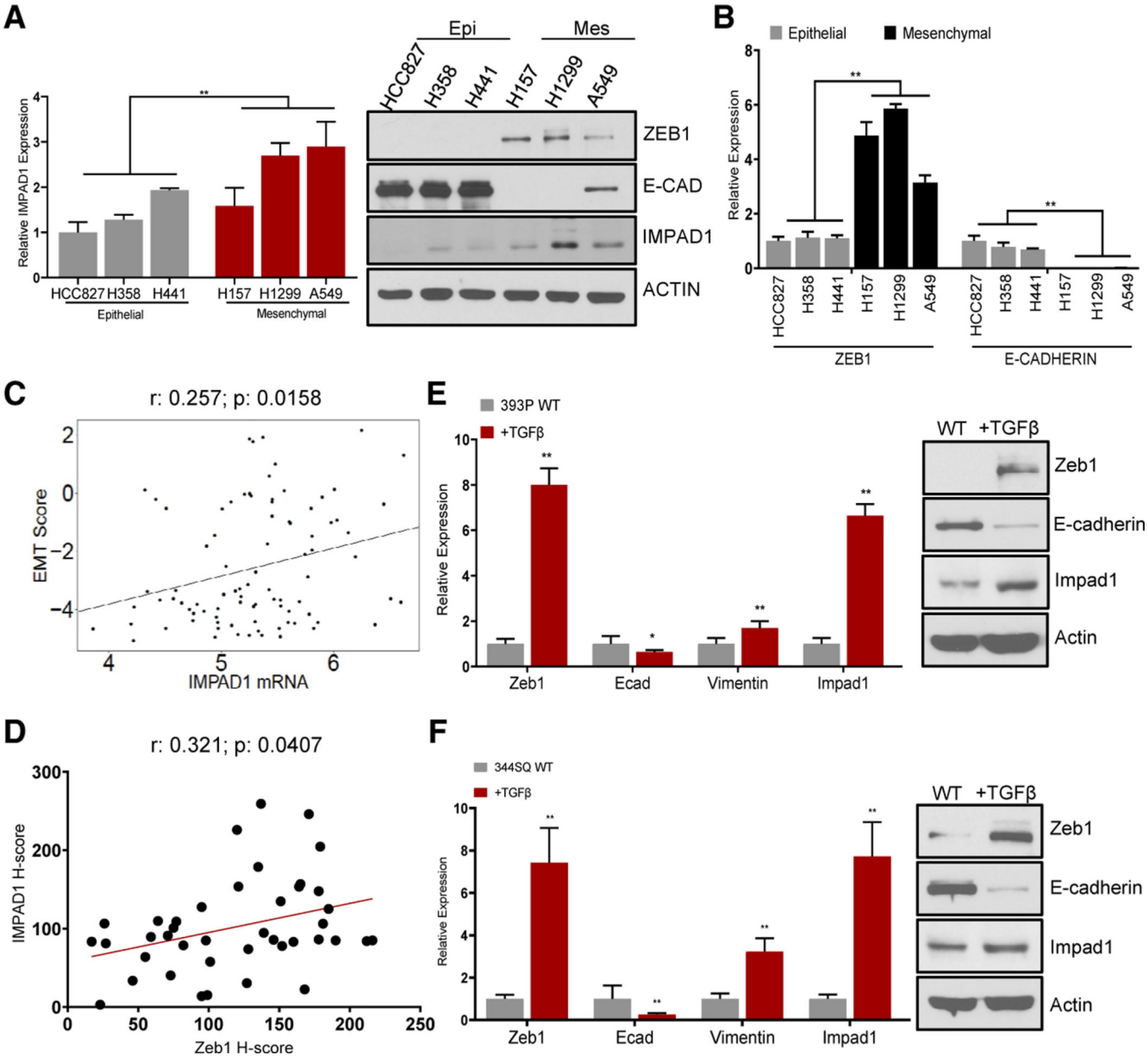

Figure 1. Impad1 is upregulated during EMT to promote tumorigenesis

(A) qPCR (left) and western blot (right) analysis of Impad1 mRNA and protein in human NSCLC models stratified based on their EMT status.

(B) mRNA levels for Zeb1 and E-cadherin in the same human NSCLC cell lines as in (A).

(C) Correlation of IMPAD1 mRNA with EMT status of human NSCLC cell lines (Spearman rho, 0.257; p = 0.0158).

(D) Correlation of IMPAD1 protein staining with ZEB1 protein levels in NSCLC whole-tissue sections from affected individuals (Spearman rho, 0.321; p = 0.0407).

(E and F) Impad1 mRNA (left) and protein (right) expression during TGF-β1-induced (5 ng/mL, day 6) EMT in murine KP cells, 393P (E) and 344SQ (F). Zeb1 and E-cadherin levels are included as markers for EMT. Actin was used as a loading control.

See also Figure S1. Data are represented as mean of triplicates ± SD. Significance by Student's t test. *$p < 0.05$; **$p < 0.002$.

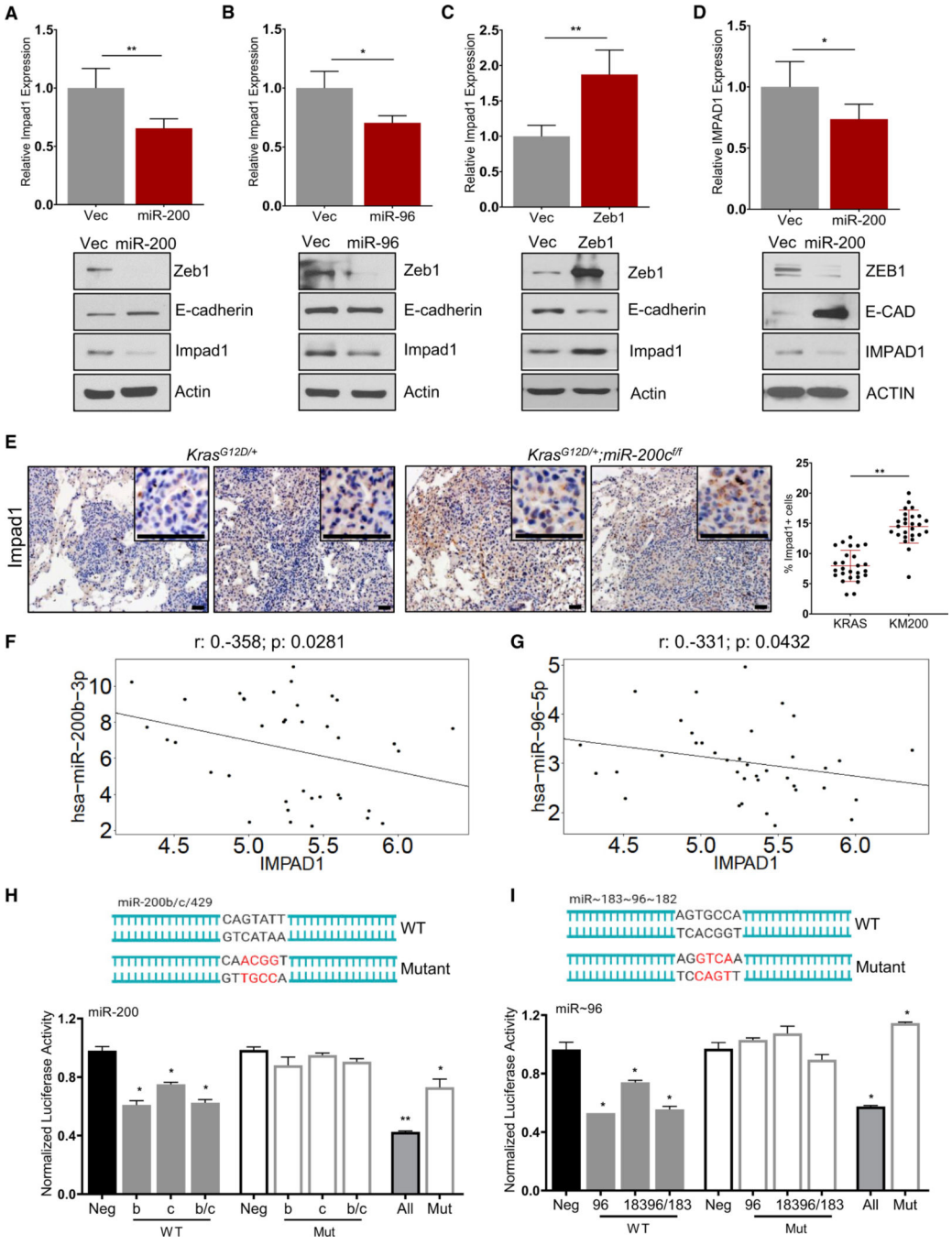

Figure 2. Impad1 is a direct target of the epithelial miRNAs miR-200 and miR~96

(A–D) Impad1 mRNA (top) and protein (bottom) expression upon miR-200 (A) or miR~96-induced (B) MET in 344SQ cells, Zeb1-induced EMT in 393P cells (C), and miR-200-induced MET in human mesenchymal lung cancer cells (H157; D) (doxycycline: 2 μM, 96 h).

(E) IHC staining and quantification for the percentage of Impad1+ cells in GEMM lung tumors (KRAS versus KM200). n = 27 (9 images/tumor). Scale bars, 20 μm). (F and G)

Correlation of Impad1 with miR-200b (F; Spearman rho, −0.358; p = 0.0281) or miR-96 (G; Spearman rho, −0.331; p = 0.0432) in human NSCLC cell lines.
(H and I) Schematic of the wild-type or mutant miRNA target sites in the Impad1 3' UTR (top). Shown is normalized luciferase reporter activity upon co-expression of the mouse control miRNA mimic or mimics for miR-200b and miR-200c (H) or mimics for miR-96 and miR-183 (I) in 393P wild-type (WT) cells. 60 pmol mimic concentration was used. See also Figure S2. Data are represented as mean ± SD. Significance by Student's t test. *p < 0.05; **p < 0.002.

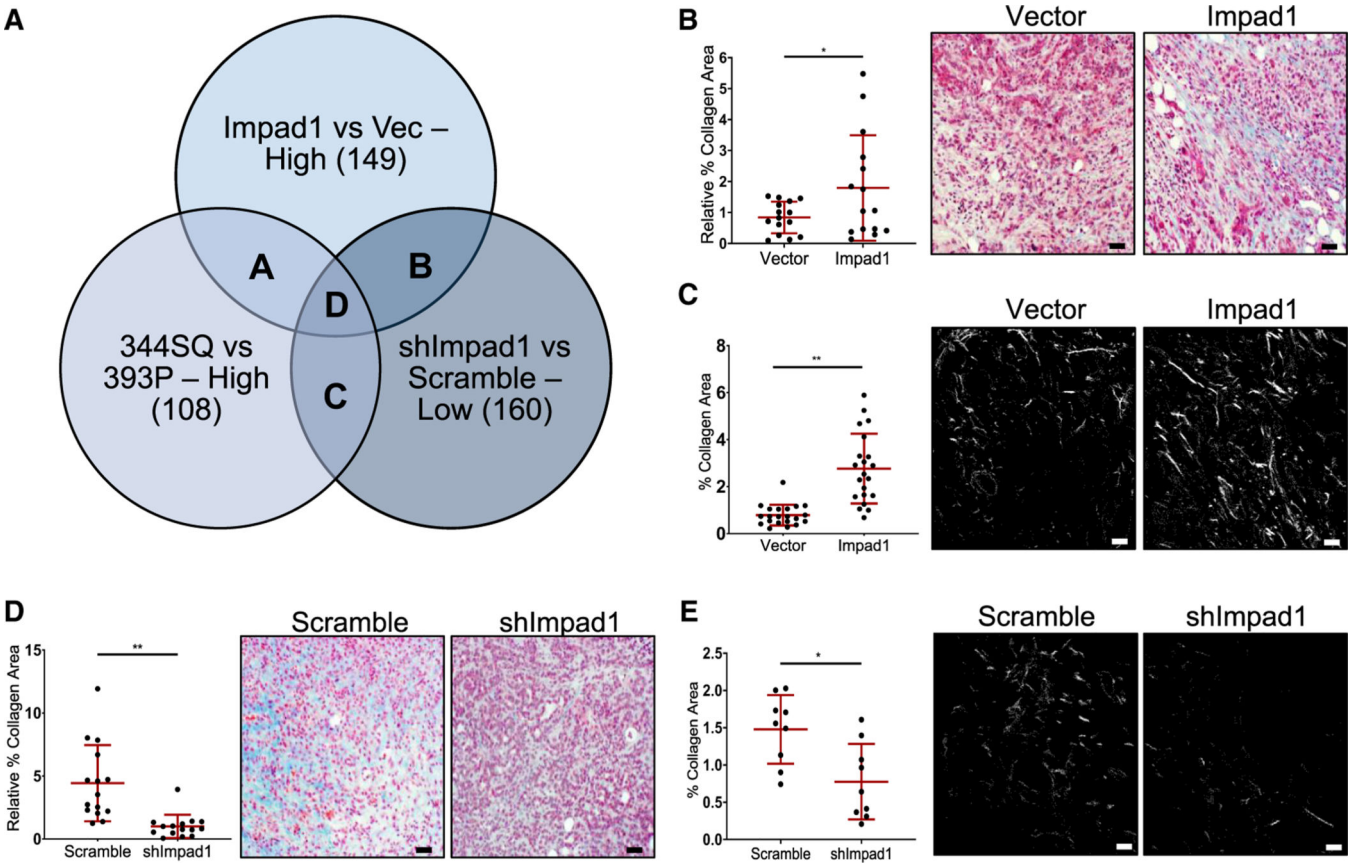

Figure 3. Impad1 alters the secretome of lung cancer cells undergoing EMT

(A) Venn diagram depicting a comparison of LC-M/MS hits from CM collected from 393P Impad1-overexpressing cells, mesenchymal 344SQ scramble control cells, and 344SQ shImpad1 cells. See also Table S1.

(B–E). Masson trichrome staining and second harmonic generation microscopy (SHG) detecting collagen in 344SQ vector or Impad1-overexpressing syngeneic tumors (B and C) and 344SQ scramble or shImpad1 knockdown syngeneic tumors (D and E). Scale bars, 50 μm.

See also Figure S3. Data are represented as mean ± SD. Significance by Student's t test. *p < 0.05; **p < 0.002.

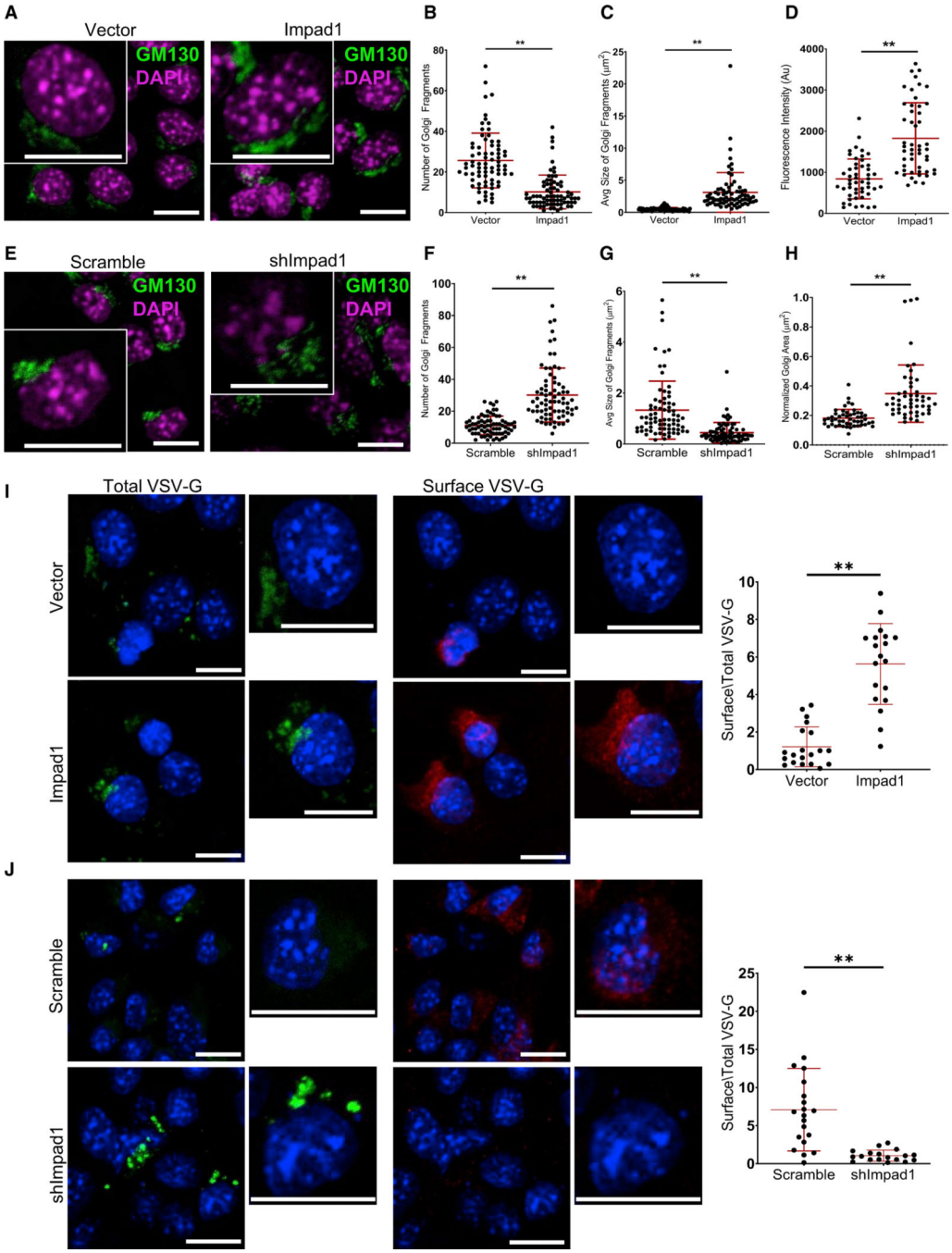

Figure 4. Impad1, a Golgi-resident protein, alters Golgi morphology and vesicular trafficking

(A–H) Confocal images of the Golgi (GM130, green) and nuclei (DAPI, magenta) in 393P vector or Impad1-overexpressing cells (A) as well as in 344SQ scramble or shImpad1 cells (E). Scatterplots show the number of Golgi fragments/cell (n = 75; B and F), average size of individual Golgi fragments/cell (n = 75; C and G), fluorescence intensity of the Golgi (n = 50; D), and normalized Golgi area (n = 50; H).

(I and J) VSV-G assay confocal images of EGFP-VSV-G-transfected 393P vector or Impad1-overexpressing cells (I) and 344SQ scramble or shImpad1 cells (J). Green, total

VSV-G; red, surface VSV-G. Scatterplots (right) show the ratio of surface to total VSV-G signal intensity/cell. n = 20; statistical outliers were removed.
Scale bars, 10 μm. See also Figure S4. Data are represented as mean ± SD. Each experiment had 3 technical replicates and 2 biological replicates. Significance by Student's t test. *$p < 0.05$; **$p < 0.002$.

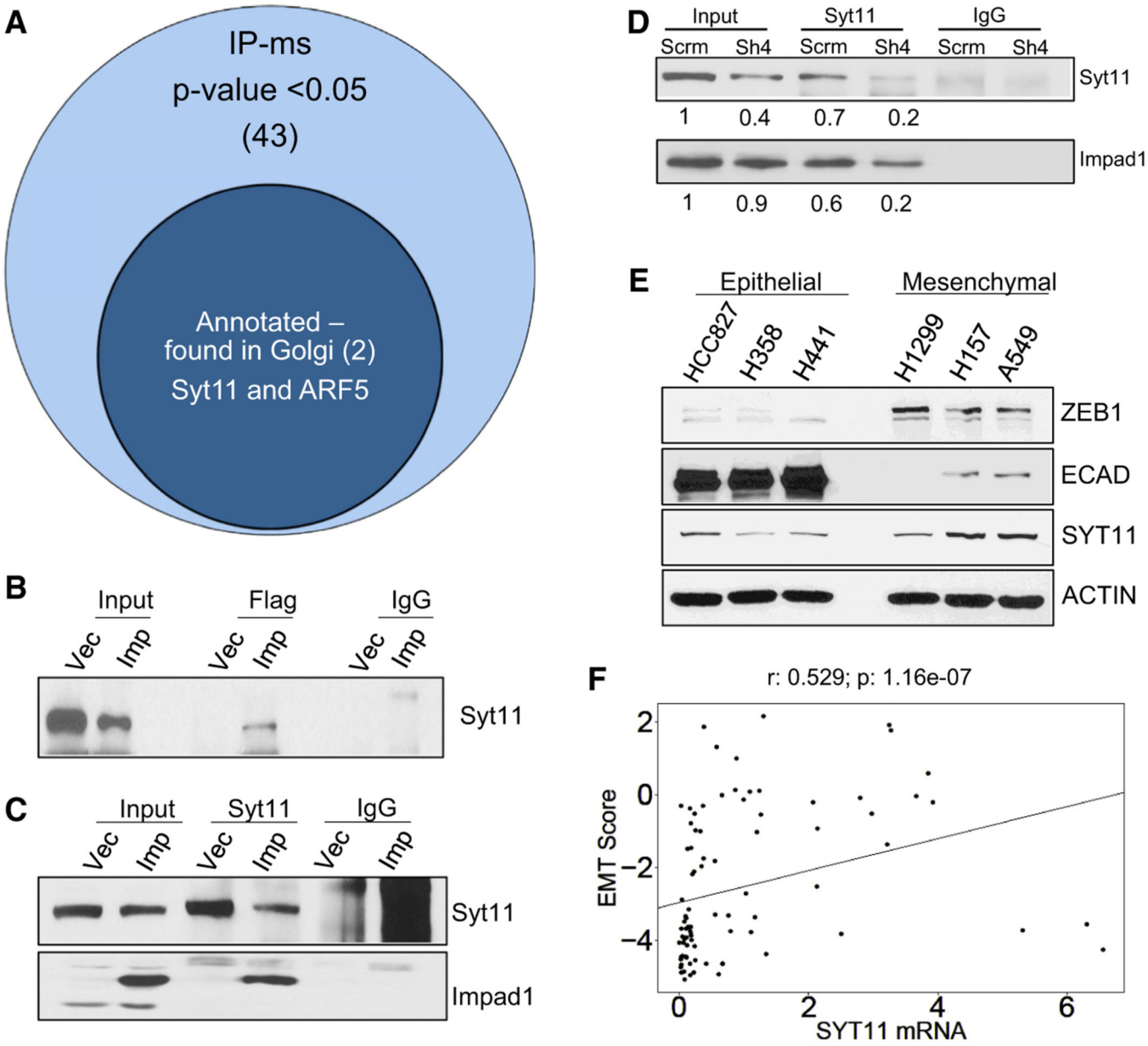

Figure 5. Impad1 interacts with another trafficking protein, Syt11

(A) Venn diagram depicting the Impad1 inter-actome identified by IP-MS analysis. See also Table S2.

(B) Probing for Syt11 upon immunoprecipitation(IP) of FLAG-Impad1 in 393P vector and Impad1overexpressing cells. Immunoglobulin G (IgG) IP was used as a negative control.

(C) Probing for Syt11 and Impad1 upon IP of Syt11 in 393P vector and Impad1-overexpressing cells.

(D) Probing for Syt11 and Impad1 upon Syt11 IP in 344SQ scramble and shSyt11 cells.

(E) Western blot analysis of Syt11 in human NSCLC cell lines distinguished by EMT status.

(F) Correlation of Syt11 with EMT score (Spearman rho, 0.529; p = 1.16e07) in human NSCLC cell lines.

See also Figure S5.

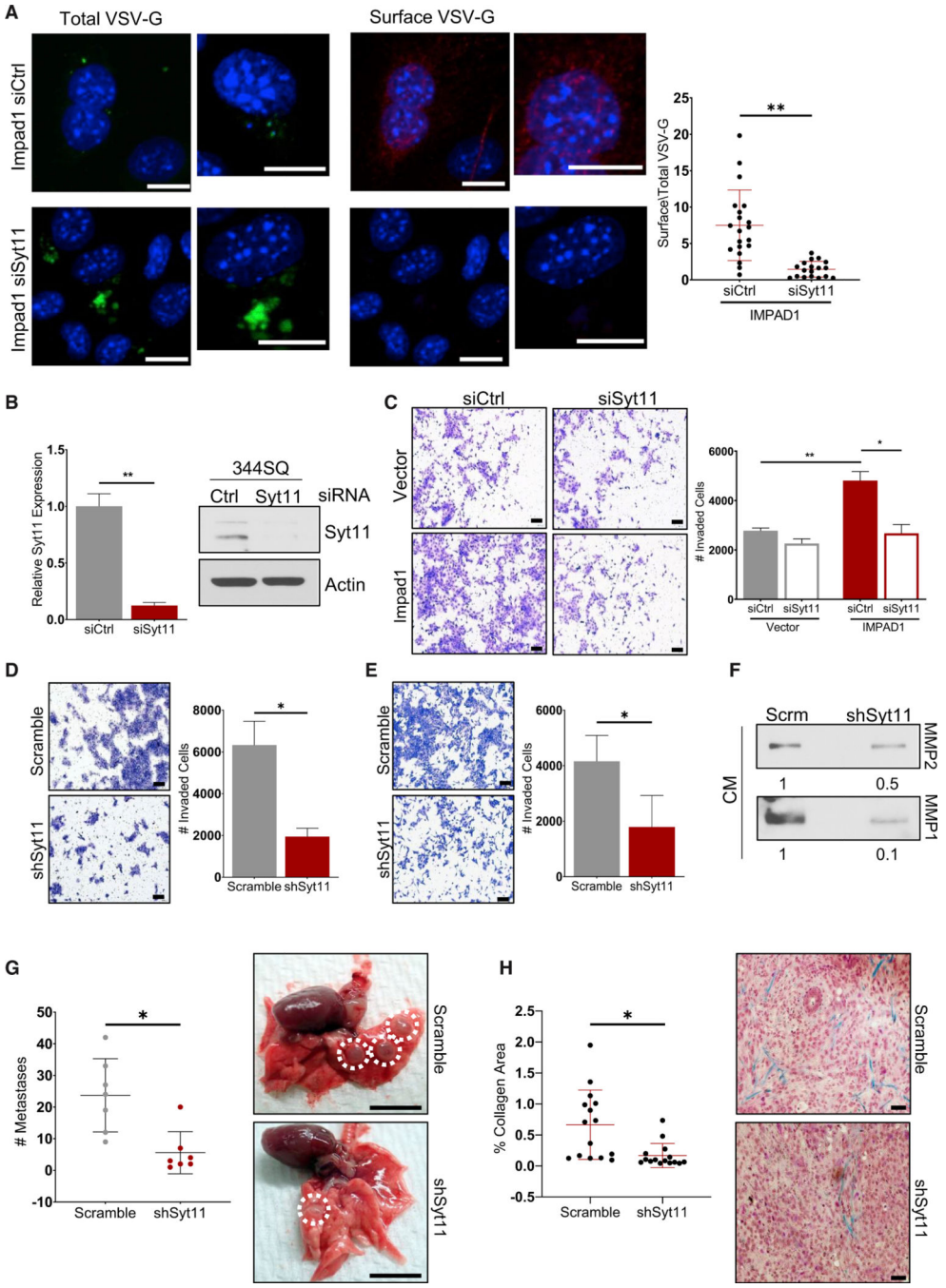

Figure 6. Syt11 is necessary to drive Impad1-mediated exocytosis, invasion, and metastasis in lung cancer

(A) VSV-G assay confocal images of 393P Impad1-overexpressing cells co-transfected with EGFP-VSV-G and siControl or siSyt11. Green, total VSV-G; red, surface VSV-G. Scatterplots (right) show the ratio of surface to total VSV-G signal intensity/cell. n = 20; statistical outliers were removed. Each experiment had 3 technical replicates and 2 biological replicates. Scale bars, 10 μm.

(B) mRNA and protein confirmation of siRNA-mediated knockdown of Syt11 in 344SQ Impad1-overexpressing cells.

(C and D) Boyden chamber assay quantifying cell invasion upon siSyt11 in 344SQ vector or Impad1-overexpressing cells. Scale bars, 100 μm.
(D) Boyden chamber assay quantifying invasion in 344SQ control or shSyt11 cells. Scale bars, 100 μm.
(E) Secretome-mediated invasion assay quantifying invasiveness of 393P KP cells replenished with conditioned medium (CM) from 344SQ scramble and shSyt11 cells. Scale bars, 100 μm.
(F) Western blot analysis of MMP1 and MMP2 in CM collected from 344SQ scramble and shSyt11 cells. Densitometric analysis of the blots was performed using ImageJ.
(G) 344SQ cells with stable Syt11 knockdown form significantly fewer lung metastatic nodules compared with the scramble control.
(H) Masson trichrome staining detecting collagen (blue) in 344SQ control and Syt11 knockdown syngeneic tumors. Scale bars, 50 μm.
See also Figure S6. Data represented as mean ± SD. Significance by Student's t test. *$p < 0.05$; **$p < 0.002$.

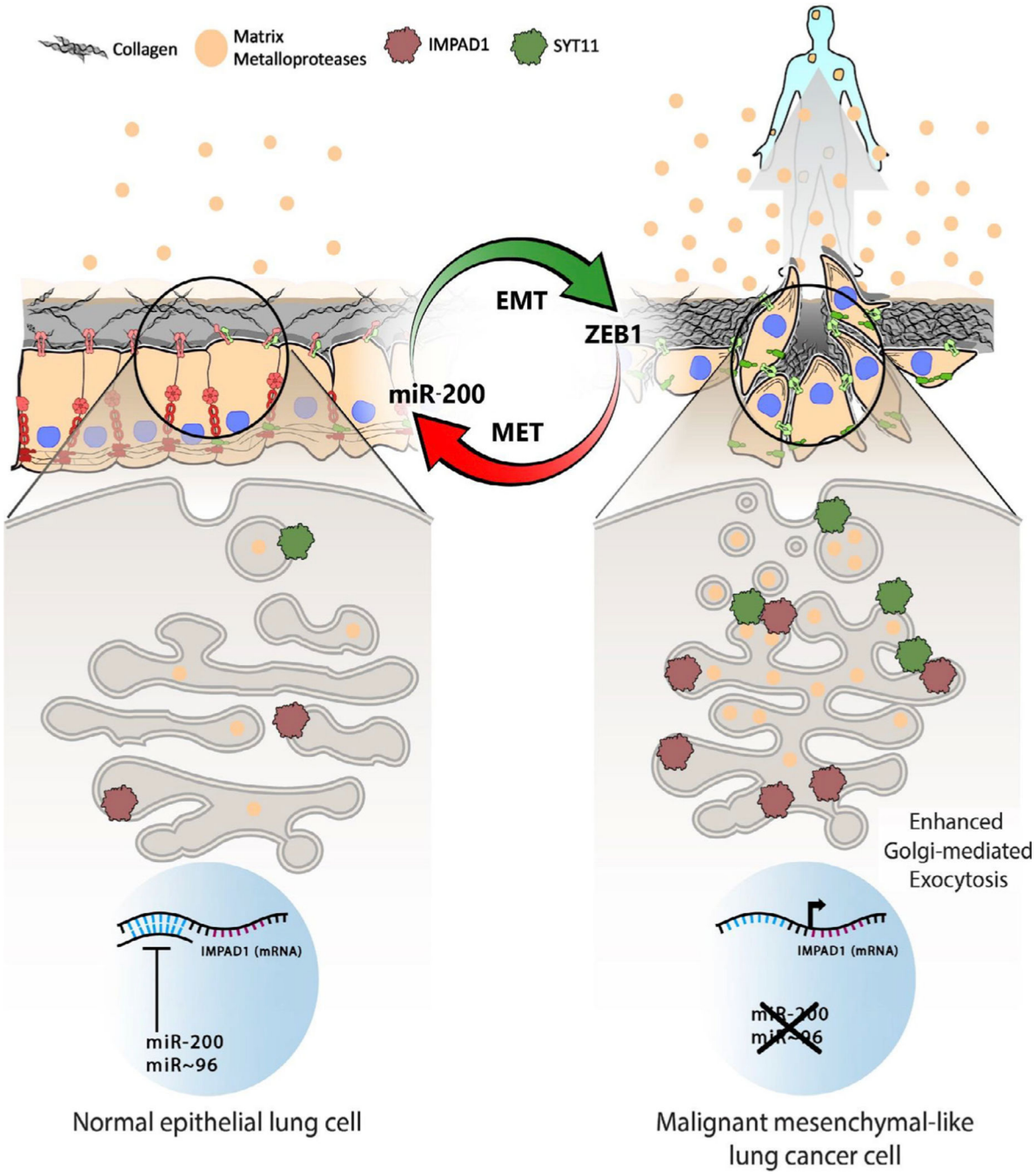

Figure 7. Working model for Impad1 modulation of Golgi morphology and vesicular trafficking to drive invasion and metastasis

Loss of the epithelial miRNAs miR-200 and miR~96 de-represses Impad1 during EMT. In mesenchymal cells, Impad1 promotes Golgi stacking and condensation as wel as vesicular trafficking in an epistatic pathway with Syt11 to enhance exocytosis of extracellular components such as MMPs, collagen, and GAGs. This increased secretion alters the ECM and TME to drive lung cancer invasion and metastasis.

KEY RESOURCES TABLE

REAGENT or RESOURCE	SOURCE	IDENTIFIER
Antibodies		
Impad1 (Mouse) (WB-1:1000, IF-1:100)	Abcam	ab69311; AB_1269163
Impad1 (Sheep) (WB-1:1000, IF-1:100, IHC-1:70)	R&D Systems	AF7028; AB_10971783
Zeb1 (Rabbit) (WB-1:500, IHC-1:200)	Genetex	GTX105278; AB_11162905
E-cadherin (Mouse) (WB-1:1000)	BD Transduction	610182; AB_397581
E-cadherin (Rabbit) (IHC-1:300)	Cell Signaling Technologies	3195; AB_2291471
Golgin97 (Rabbit) (WB-1:1000, IF-1:1000)	Cell Signaling Technologies	13192; AB_2798144
GM130 (Rabbit) (WB-1:1000)	Cell Signaling Technologies	12480; AB_2797933
GM130 (Mouse) (IF-1:80)	BD Biosciences	560257; AB_1645351
Syt11 (Rabbit) (WB-1:1000, IF-1:1000, IP-2ug)	Thermofisher	PA5-96970; AB_2808772
Arf5 (Rabbit) (WB-1:500)	Proteintech	20227-1-AP; AB_10639517
MMP-1 (Rabbit) (WB-1:1000)	Genetex	GTX100534; AB_1950926
MMP-2 (Rabbit) (WB-1:1000)	Cell Signaling Technologies	87809; AB_2800107
Integrin-α6 (Rabbit) (WB-1:1000)	Cell Signaling Technologies	3750; AB_2249263
β-Actin (Mouse) (WB-1:10,000)	Proteintech	66009-1; AB_2687938
VSV-G (Mouse) (VSV-G-1:100)	Kerafast	EB0012
Anti-Mouse(WB-1:2000)	Cell Signaling Technologies	7076; AB_330924
Anti-Rabbit(WB-1:2000)	Cell Signaling Technologies	7074; AB_2099233
Anti-Sheep(WB-1:2000)	Abcam	ab6900; AB_955452
Alexa 546 anti-mouse(IF-1:200)	Thermofisher Scientific	A11030; AB_2534089
Alexa 488 anti-rabbit(IF-1:200)	Thermofisher Scientific	A11008; AB_2534089
Alexa 635 anti-rabbit(IF-1:200)	Thermofisher Scientific	A31576; AB_2536186
Alexa 546 anti-sheep(IF-1:200)	Thermofisher Scientific	A21098; AB_2535752
Alexa 568 anti-mouse(VSV-G/IF-1:200)	Thermofisher Scientific	A10037; AB_2534013
Anti-Rabbit(IHC-1:300)	Dako	E0353; AB_2737292
Anti-Mouse(IHC-1:150)	Abcam	ab6746; AB_954917
CD8 PE-Cy7 (53-6.7) (Flow-1:800)	BioLegend	100721; AB_312760
CD3 PE-594 (17A2) (Flow-1:100)	BioLegend	100246; AB_2565883
CD62L FITC (MEL-14) (Flow-1:100)	Tonbo	35-0621-U500; AB_2621697
CD274 PE-594 (10F.9G2) (Flow-1:100)	BioLegend	124323; AB_2565638
CD44 APC (IM7) (Flow-1:100)	BioLegend	103012; AB_312963
CD4 APC-Cy7 (RM4-5) (Flow-1:100)	BioLegend	100526; AB_312727
FoxP3 PerCp-Cy5.5 (FJK-16s) (Flow-1:100)	eBioscience	45-5773-82; AB_914351
CD86 APC-Cy7 (GL-1) (Flow-1:100)	BioLegend	105030; AB_2244452
CD68 PerCp-Cy5.5 (FA-11) (Flow-1:100)	BioLegend	137009; AB_10575455
CD69 BV650 (H1.2F3) (Flow-1:100)	BioLegend	104541; AB_2616934
CD45 Pacific Blue (30-F11) (Flow-1:100)	BioLegend	103126; AB_493535
CD45 PerCp-Cy5.5(Flow-1:100)	BioLegend	103132; AB_893340
CD25 BUV395 (PC61) (Flow-1:100)	BD Biosciences	564022; AB_2722574

REAGENT or RESOURCE	SOURCE	IDENTIFIER
CD11c BV786 (N418) (Flow-1:100)	BioLegend	117335; AB_11219204
CD44 BV711 (IM7) (Flow-1:100)	BioLegend	103057; AB_2564214
GR1 BV711 (RB6-8C5) (Flow-1:100)	BioLegend	108443; AB_2562549
CD278 PE (7E.17G9) (Flow-1:100)	BioLegend	117406; AB_2122712
CD278 BV785 (C398.4A) (Flow-1:100)	BioLegend	313533; AB_2629728
TIM3 APC (B8.2c12) (Flow-1:100)	BioLegend	134007; AB_2562997
PD1 BV605 (29F.1A12) (Flow-1:100)	BioLegend	135220; AB_2562616
PD-1 FITC (29F.1A12) (Flow-1:100)	BioLegend	135214; AB_10680238
F4/80 APC (BM8.1) (Flow-1:100)	Tonbo	20-4801-U100; AB_2621602
MHC II/PE-Cy (M5/114.15.2) (Flow-1:100)	BioLegend	107629; AB_2290801
CD11b BV650 (M1170) (Flow-1:100)	BioLegend	101239; AB_11125575
CD206-FITC(Flow-1:100)	BioLegend	141703; AB_10900988
CD36-PE(Flow-1:100)	BioLegend	102605; AB_389348
Oligonucleotides		
IMPAD1-FCCGCAAGATGTTCTACCTGCTCqPCR Murine	This paper	N/A
IMPAD1-RGATGTCCTCAGGAATCTTCCGqPCR Murine	This paper	N/A
Zeb1-FATGCTCTGAACGCGCAGCqPCR Murine	This paper	N/A
Zeb1-RAATCGGCGATCTTTGAGAGCTqPCR Murine	This paper	N/A
E-cadherin-FGTCATCAGTGTGCTCACCTCTqPCR Murine	This paper	N/A
E-cadherin-RCTGTTGTGCTCAAGCCTTCACqPCR Murine	This paper	N/A
Vimentin-FGGAAAGTGGAATCCTTGCAGGqPCR Murine	This paper	N/A
Vimentin-RGCAGTGAGGTCAGGCTTGGAAqPCR Murine	This paper	N/A
Syt11-FAATGCGTTTTCTGCCGTAGTAGAqPCR Murine	This paper	N/A
Syt11-RTGACCAGGGACATCATCAAGAGqPCR Murine	This paper	N/A
Software and algorithms		
TargetScan	https://www.targetscan.org/vert_80/	Murine and Human datasets were used.